Validation of geostationary operational environmental satellite-16 advanced baseline imager radiometric calibration with airborne field campaign data and reanalysis of north-south scan data

Xi Shao[a,*] **Francis P. Padula**[b] **Changyong Cao**[c] **Xiangqian Wu**[c] **Fangfang Yu**[a] **Aaron Pearlman**[b] **Haifeng Qian**[a] **Sirish Uprety**[a] **and Taeyoung Choi**[d]

[a]University of Maryland, Cooperative Institute for Satellite Earth System Studies (CISESS), Earth System Science Interdisciplinary Research Center, College Park, Maryland, United States

[b]GeoThinkTank LLC., Washington, DC, United States

[c]NOAA, Center for Satellite Applications and Research, College Park, Maryland, United States

[d]Global Science & Technology, Inc., Greenbelt, Maryland, United States

Abstract. The advanced baseline imager (ABI) on board geostationary operational environmental satellite-16 (GOES-16) provides high quality reflective solar band (RSB) and thermal emission band (TEB) image data. Intensive field campaigns for postlaunch validation of the ABI Level-1B spectral radiance observations were carried out during March to May of 2017 to ensure the Système International traceability of the ABI. Radiometric calibrations of the RSBs and TEBs of the ABI were evaluated by comparison with the spectral measurements of the airborne visible infrared imaging spectrometer-next generation (AVIRIS-NG) and scanning high-resolution interferometer sounder (S-HIS) on board the high-altitude aircraft ER2, respectively. The comparison between ABI RSB mesoscale (MESO) data and AVIRIS-NG measurements showed that the mean biases are within 2% with uncertainty <2.5% for ABI CH01, CH03, CH05, and CH06. The brightness temperature differences between GOES-16 ABI and S-HIS measurements were shown to be within 0.45 K with uncertainty <0.35 K at the 300 K scene equivalent for ABI CH08 to CH10 and CH13 to CH15. The ABI uses large focal plane arrays with the detector number varying from hundreds to more than a thousand per channel, which makes the evaluation of detector uniformity a challenge. Reanalysis of the GOES-16 ABI north-south scan data from the field campaign and lunar observation was performed for ABI CH01 to CH03 with two versions of calibration coefficients. Significant improvements in detector uniformity with the updated solar calibration algorithm were verified. [DOI: 10.1117/1.JRS.16.037501]

Keywords: geostationary operational environmental satellite-16; advanced baseline imager; radiometric calibration; Système International traceability; airborne visible infrared imaging spectrometer – next generation; scanning high-resolution interferometer sounder; north-south scan; airborne field campaign; detector uniformity.

Paper 210714G received Nov. 4, 2021; accepted for publication Jul. 5, 2022; published online Jul. 21, 2022.

1 Introduction

Being the first satellite in the latest generation of geostationary earth-observing systems, geostationary operational environmental satellite-16 (GOES-16) (formerly known as GOES-R before reaching the geostationary orbit) of National Oceanic and Atmospheric Administration (NOAA) was successfully launched on November 19, 2016.[1–9] The GOES-16 was in operation

*Address all correspondence to Xi Shao, xshao@umd.edu

initially at around 89.3-deg and 89.5-deg west longitude, where it underwent an extended testing and validation phase and then moved to 75.2-deg west longitude as GOES-east on December 18, 2017, to cover the eastern American continental regions. After the successful operation of GOES-16, GOES-17 was launched on March 1, 2018,[10,11] and became operational as GOES-west at 137.2-deg west longitude on February 12, 2019.

The GOES-16 advanced baseline imager (ABI) provides high spatial and temporal resolution imagery of the Earth through 16 spectral bands at visible and infrared wavelengths. The ABI provides image products with up to four times greater spatial resolution and five times greater temporal resolution in comparison with the previous GOES imager. ABI data are critical for a wide range of applications related to weather forecasting, environmental monitoring, ocean and land studies, climate, hazards (fires, volcanoes, floods, hurricanes, storms, and tornadoes), and disaster relief. The radiometric accuracy and consistency of ABI are particularly important for these applications. It is critical to ensure that the radiometric accuracy of ABI is within the specs and is traceable. The radiometric accuracy for the ABI reflective solar band (RSB) (CH01 to CH06) is required to be within 5%, which is achieved through onboard radiometric calibration using a solar diffuser. The accuracy requirement of 5% is interpreted here as the 1 sigma (or $k = 1$) total radiometric uncertainty including noise, calibration, etc. For thermal emission bands (TEBs) of GOES-16 ABI, the requirement for radiometric accuracy is to be within 1 K (1 sigma or $k = 1$), which is maintained through onboard calibration using a blackbody.

As part of the comprehensive postlaunch validation activities for the GOES-16 ABI, intensive airborne science validation field campaigns were carried out from March to May of 2017 to support the validation of ABI level-1B radiance products. Field campaigns are internationally recognized as a best practice by the committee on Earth observation satellites (CEOS)[12] and global space-based intercalibration system (GSICS)[13] to ensure the postlaunch instrument performance. During the field campaign, the flight path and scheduling of the NASA ER-2 high-altitude airborne science aircraft were coordinated with the timeline 25 special scans of the GOES-16 ABI.[14–18] Both the airborne visible infrared imaging spectrometer – next generation (AVIRIS-NG) and the scanning high-resolution interferometer sounder (S-HIS) instruments were on board the NASA ER-2 aircraft to collect spectral measurements over the target regions. In particular, AVIRIS-NG provides high signal-to-noise ratio (SNR) imaging spectroscopy measurements in the solar reflected spectral range,[19–22] which validate the ABI RSB observations. AVIRIS-NG has Système International (SI) traceability to the National Institute of Standard Technology (NIST) via a tungsten coiled filament (FEL) lamp. S-HIS is a Fourier transform spectrometer (FTS)[23–26] that measures thermal radiation at high-spectral resolution. It has SI traceability to the NIST thermal infrared transfer radiometer (TXR). The comparison with the S-HIS measurements provides radiometric uncertainty evaluation for GOES-16 ABI TEBs.

In this paper, comparisons between GOES-16 ABI timeline 25 MESO scene observations and the coordinated AVIRIS-NG and S-HIS measurements during the field campaign of the Sonoran Desert and surrounding area on March 28, 2017, are performed. In the ABI terms, a timeline defines an ABI scan mode that normally consists of different types of scans covering various sizes of regions by scanning from west to east in a raster pattern with differing numbers of swaths: full disk images consist of 22 swaths, Continental US (CONUS) images consist of six swaths, and mesoscale (MESO) images consist of two swaths. A special scan mode (timeline 25) was created for the field campaign, however, that includes nominal MESO scans as well as so-called north-south scans (NSS) (that place each channel's detectors over the same nominal location using a sequence of scans in the north-south direction) to cover a small region with a high temporal cadence.

In this paper, the overall radiometric performance of ABI RSBs in comparison with the ray-matched AVIRIS-NG measurements is presented. The brightness temperature (BT) differences between GOES-16 ABI TEB and S-HIS measurements over ray-matching land targets are also evaluated. Through comparison with the coordinated SI-traceable airborne spectral radiance measurements by AVIRIS-NG and S-HIS, the SI traceability of the ABI level-1B observations is independently validated. It is noted that earlier work in Ref. 17 compared the GOES-16 ABI NSS field campaign data with AVIRIS-NG measurements for radiometric validation of ABI RSB channel performance. In Ref. 27, the ABI TEB observations at night over an ocean target in the Gulf of Mexico were compared with simultaneous S-HIS measurements for the validation of the

ABI TEBs using S-HIS. The focus of this work is to evaluate the radiometric performance of ABI MESO scans over the Sonoran Desert for both RSBs and TEBs of the GOES-16 ABI.

The ABI uses large focal plane detector arrays with 100 to >1400 detectors, which increase the system's sensitivity to image striping (detector-to-detector nonuniformities). Ensuring the radiometric uniformity among such a large number of detectors for each channel of the ABI poses a significant challenge to the calibration. During the early on-orbit, there were several implementations and updates of the ABI solar calibration algorithms to account for the integration time difference between solar calibration and Earth view, which result in different versions of detector gains and consequently different radiance and detector uniformity performance. Also, right before the field campaign, the nonlinear calibration factor table was updated for ABI CH01 to CH03 for image striping mitigation. The impacts of such calibration updates need to be evaluated along with the overall independent validation of the system.

Each ABI RSB channel has 100 to 1000 detector rows, and each row consists of three or six detector columns. In operation, only one detector column of data in each row is downlinked for operational processing of Earth view data on the ground. The NSS of ABI was designed to have all of the detectors on different rows, but the same column of detector array for a given channel collects the data over the same target region. These acquisitions were conducted in rapid succession, such that the scene changes are expected to be negligible. The detector uniformity performance for each channel is then evaluated by intercomparing the target radiance among detectors. In this paper, the GOES-16 ABI CH01 to CH03 NSS data collected during the field campaign and lunar observation are analyzed with calibration coefficients derived from two calibration algorithms. The impacts on the detector uniformity from the implementation of the updated nonlinear calibration factor and integration time change in solar calibration are quantitatively evaluated.

The paper is organized as follows. In Sec. 2, the radiometric biases of GOES-16 ABI RSB channels are evaluated through comparison with the AVIRIS-NG measurements over the Sonoran Desert region collected during the field campaign. In Sec. 3, the GOES-16 ABI TEB data are compared with the S-HIS measurements to evaluate the radiometric biases of ABI TEBs. In Sec. 4, the detector uniformity of GOES-16 ABI CH01 to CH03 is evaluated with both NSS data collected during the field campaign and lunar observation data, which are processed with two calibration algorithms. Section 5 presents the overall summary of the validation of the radiometric calibration of GOES-16 ABI RSB and TEB with the airborne field campaign data and reanalysis of NSS data.

2 Radiometric Comparison Between GOES-16 ABI MESO Scene and AVIRIS-NG Measurement

2.1 *GOES-16 ABI and AVIRIS-NG RSB Data Collection During Field Campaign*

GOES-16 ABI has six RSB channels covering a spectral range from 0.47 to 2.25 μm with a spatial resolution varying from 0.5 to 2.0 km. Table 1 summarizes the detailed specifications of ABI RSB channels. The ABI RSB channel data collection during the field campaign on March 28, 2017, was executed under timeline 25 scheduling with the GOES-16 nadir checkout location being at −89.5°W. Each timeline 25 mode has a 5-min duration. During the timeline 25 mode of ABI, MESO scans were performed. Each ABI MESO scan consists of two swaths covering the Sonoran Desert region where simultaneous air-borne reference sensor measurements were performed during the field campaign. This MESO scan was repeated 10 times during each timeline 25 operation, and data were collected for each of the ABI channels.

AVIRIS-NG was developed following the legacy AVIRIS to provide continued access to high SNR imaging spectroscopy measurements in the solar reflected spectral range.[19–22] It measures the wavelength range from 380 to 2510 nm with 5-nm sampling. Spectra of AVIRIS-NG are measured as images with 600 cross-track elements at a spatial sampling of 1.0 ± 0.1 mrad. AVIRIS-NG has better than 97% cross-track spectral uniformity and ≥97% spectral instantaneous field of view (IFOV) uniformity. AVIRIS-NG has an onboard calibrator source and

Table 1 ABI RSB channel specifications.

ABI channel	Wavelength (μm)	Resolution (km)	Detector number	Detector columns
1	0.47	1	676	3
2	0.64	0.5	1460	3
3	0.87	1	676	3
4	1.38	2	372	6
5	1.61	1	676	6
6	2.26	2	372	6

maintains <3% uncertainty with SI traceability to NIST via a FEL lamp. The FEL lamp along with an integrating sphere for absolute calibration is used for preflight calibration of AVIRIS-NG. An on-board source is used to detect any gross changes and correct for local striping effects. This calibration process is described in more detail in Ref. 22. The in-flight radiance was validated during the same Sonoran Desert flights in the GOES-R field campaign by also flying over an Ivanpah desert site where a NASA Jet Propulsion Laboratory ground team performed ground validation. AVIRIS-NG has an FOV of 34 deg. The spatial swath of AVIRIS-NG is ~11 km with a spatial resolution of ~20 m at a typical altitude of 20 km for ER2 aircraft.

On March 28, 2017, the targeted field campaign location was placed around the Sonoran Desert region with ~90 min coordinated data collection by AVIRIS-NG on board the ER-2 aircraft. Figure 1 shows the ground track of the ER-2 aircraft on March 28, 2017. About eight circular flight ground tracks were designed and carried out over the region of the Sonoran Desert to ensure that the view geometry of AVIRIS-NG matched that of ABI over the target region. AVIRIS-NG scans as far as 34 deg off-nadir. Thus, with the addition of a ~33 deg bank angle from the ER-2 aircraft, it enables a match of the ABI view geometry over the target location.

The ABI timeline 25 special scan data collected during the field campaign need to be calibrated and navigated. The ABI MESO data used in this paper were specially processed by the instrument vendor, i.e., so-called Pleiades version. In the Pleiades version of reprocessed ABI RSB data, solar calibration to derive the detector gain factor, processing of the raw data to radiance data, and image navigation were all performed by the ABI vendor. Figure 2 shows an example of the radiance map from (a) AVIRIS-NG data and (b) ABI-Pleiades version data for ABI CH02 on March 28, 2017. Note that the AVIRIS-NG radiance measurements were recorded

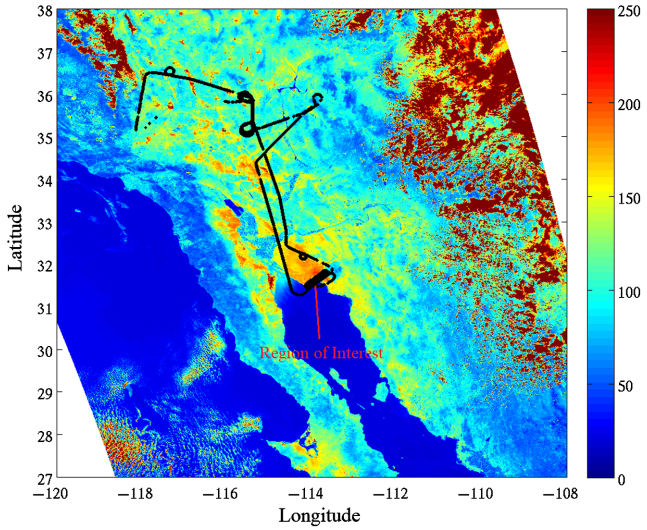

Fig. 1 Ground track of ER-2 (black line) overlaid on GOES-16 ABI CH02 radiance (W/m^2-sr-μm) image during the field campaign on March 28, 2017.

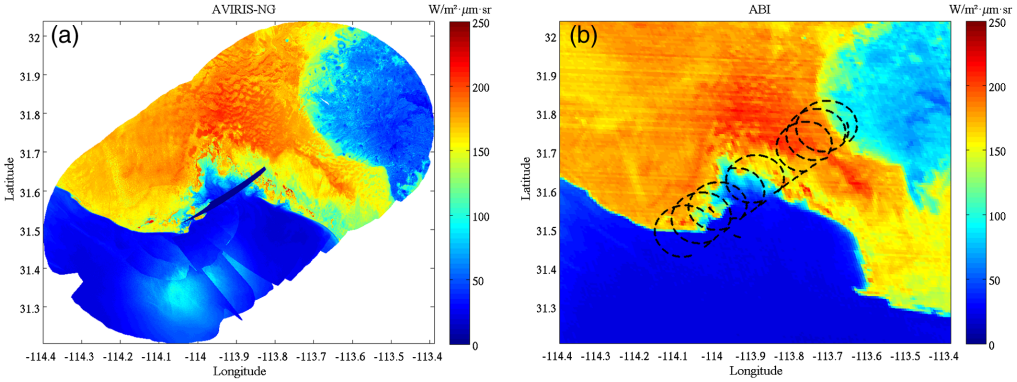

Fig. 2 Processed (a) AVIRIS-NG radiance map and (b) ABI observation for GOES-16 ABI CH02 during the field campaign on March 28, 2017. The dark blue area in the left panel indicates the gap in the AVIRIS coverage. The black dashed line in the right panel marks the ground track of the ER-2 aircraft overlaid on the GOES-16 CH02 radiance map during the March 28, 2017, field campaign.

with the unit $\mu W/cm^2$-nm-sr, and we have converted the data to have the same standard radiance unit (W/m^2-μm-sr) as the ABI measurement. The AVIRIS-NG hyperspectral data were convolved with the spectral response function (SRF) of ABI CH02, i.e., GOES-R calibration working group flight module 1 (FM1) SRF release v3.[28] In this way, the effective AVIRIS-NG spectral radiance over the ABI CH02 band is calculated. Note that AVIRIS-NG data was accumulated over approximately an hour on March 28, and the ABI data is from one snapshot of the MESO scene scan. The overall radiance maps derived from AVIRIS-NG and ABI measurements are consistent. The difference between the two panels is mainly due to several factors such as different sensor view angles and data collection over ~60- min period for AVIRIS-NG versus a snapshot for ABI. A more precise radiometric comparison between ABI and AVIRIS-NG measurements requires the matching in view geometry and time between these two sensors.

2.2 *Ray-Matching Between GOES-16 ABI and AVIRIS-NG Measurements*

To determine the radiance difference between GOES-16 ABI and AVIRIS-NG for a given ABI RSB channel, identifying optimally matched view geometry samples between ABI and AVIRIS-NG sensor both in time and space is required. The following ray-matching conditions were applied in searching for the qualified matching locations.

1. For the region of interest (RoI), the view angle between the ABI line of sight and the AVIRIS-NG line of sight should be within 5 deg. AVIRIS-NG can scan as far as 34 deg off-nadir, which made it easy to match the ABI view geometry over the target location during the circular flight paths on March 28, 2017. Because GOES-16 nadir view is fixed at −89.5°W during the field campaign, the view angle of ABI w.r.t. the pixel map of AVIRIS-NG can be readily calculated. Figure 3 shows the map of the angle between the ABI view vector and the AVIRIS-NG view vector for each pixel of AVIRIS-NG measurement during the field campaign on March 28, 2017. In Fig. 3, the blue-shaded regions with angle <5 deg mark where the ray-matching condition is satisfied during the circular flight paths of the ER-2 aircraft. The threshold for the ray-matching cone angle is chosen as a balance between keeping enough matched data points for all of ABI RSB channels and confining the ray-matching angle as small as possible. The ABI CH06 has the largest nadir grid spacing of 2 km. There are about nine ABI CH06 data points within the 5-deg matched cone angle, which makes the comparison statistically significant while maintaining minimum view angle differences.
2. Temporal matching was enforced so that the time difference between the GOES-16 ABI observation and AVIRIS-NG measurement over the RoI was within 30 s. The ABI MESO mode scans through the region every 30 s, and the time stamp of AVIRIS-NG measurement over the RoI is used to find the closest ABI MESO data in time that constrains the time difference to be within 30 s.

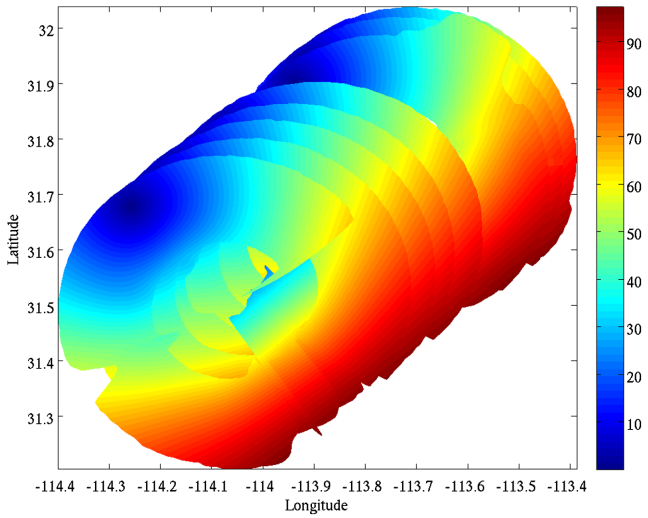

Fig. 3 Color map of angle (degree) between GOES-16 ABI view vector and AVIRIS-NG view vector during the field campaign on March 28, 2017. The blue-shaded regions with minimum angle (<5 deg) are where the ray-matching condition is satisfied.

There are eight locations in total within the circular paths of the ER-2 aircraft that satisfy the ray-matching condition. Figure 4 shows the processed AVIRIS-NG radiance data for ABI CH01, CH02, CH03, and CH06 over the eight selected RoIs around the Sonoran Desert region. The AVIRIS-NG hyperspectral radiance data were convolved with the corresponding ABI SRFs to derive the radiance for each ABI RSB channel. Due to the much higher spatial resolutions of AVIRIS-NG measurements, the radiance maps over the eight sites show abundant spatial

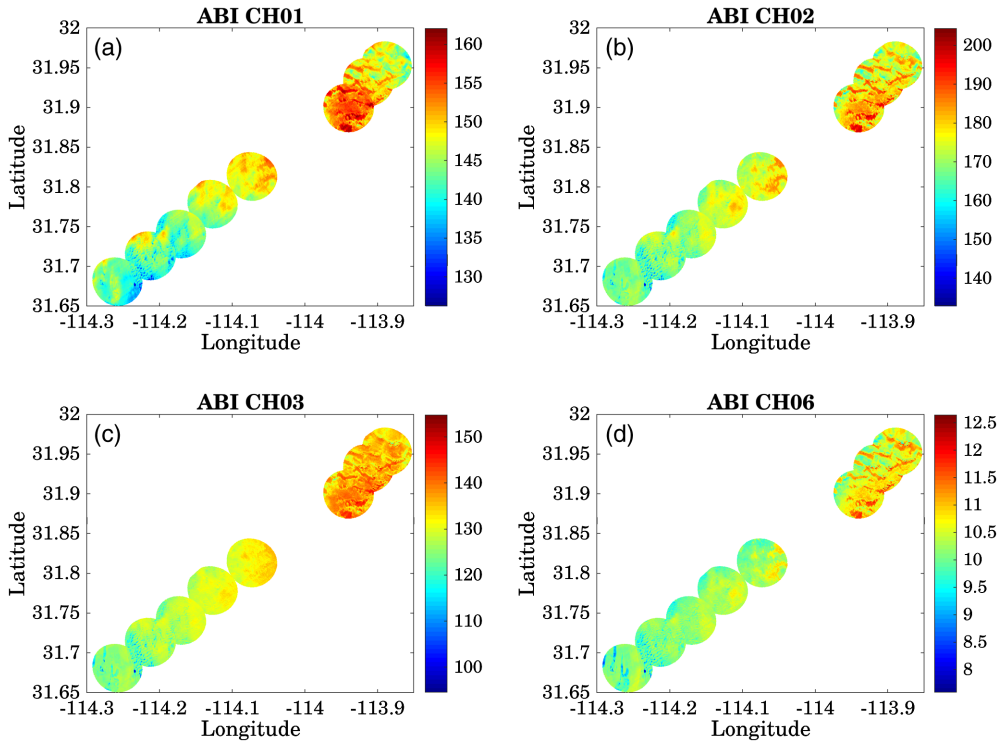

Fig. 4 (a)–(d) Derived AVIRIS-NG radiance (W/m^2-sr-μm) data for ABI CH01, CH02, CH03, and CH06, respectively, over the eight selected RoIs that satisfy the ray-matching condition. Convolution was applied to the AVIRIS-NG data with the corresponding SRFs of ABI channels.

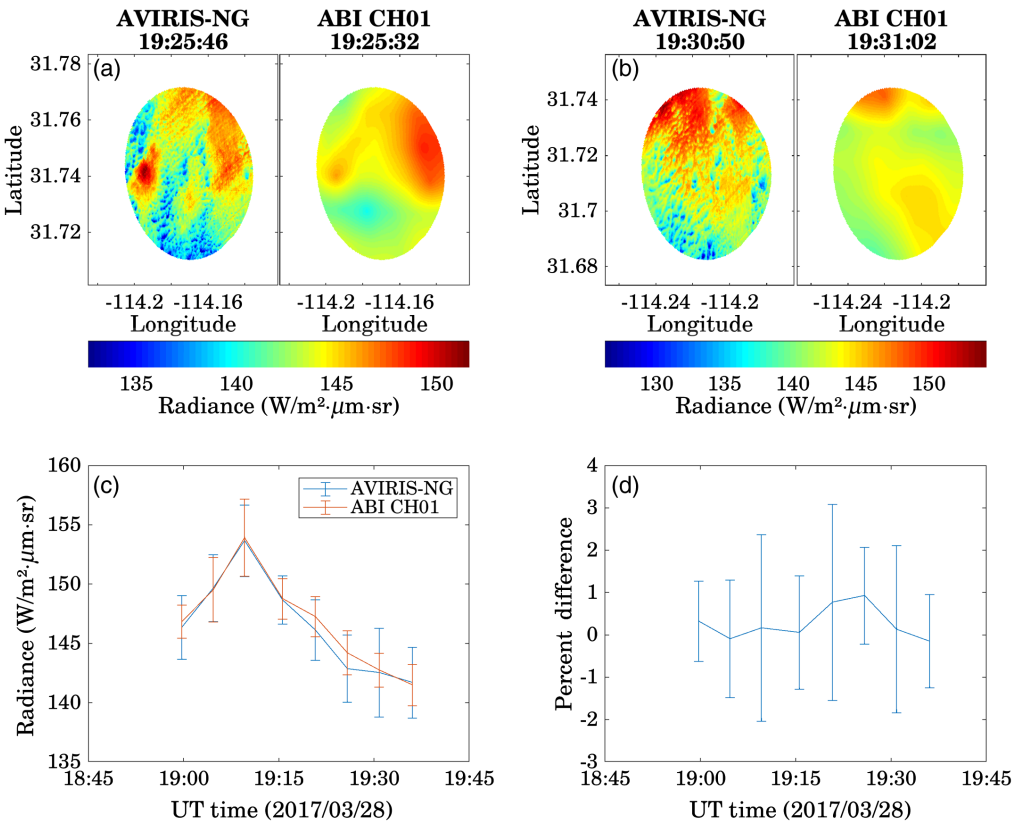

Fig. 5 (a) and (b) Selected comparison between sampled GOES-16 ABI MESO and AVIRIS-NG data over two ray-matching sites (<5 deg) during March 28, 2017, for ABI CH01. The AVIRIS-NG data were convolved with the SRF of ABI CH01. ABI MESO data was sampled into the 5-deg ray-matching region. (c) Time series of mean radiance over the ray-matching sites derived from GOES-16 ABI MESO and AVIRIS-NG measurements for ABI CH01. Vertical bars indicate the standard deviation of scene radiance due to scene nonuniformity. (d) Time series of percent difference between the mean radiances of ABI and AVIRIS-NG over the ray-matching sites for ABI CH01. The error bars mark the one-sigma standard deviation ($k = 1$) of the percent differences.

variations, which indicate that the AVIRIS-NG measurements cover a variety of land types with substantial features.

Figures 5–7 show example comparisons of the measured radiance between the ABI and AVIRIS-NG for ABI CH01 to CH03, respectively. The top panels show the selected comparison between sampled AVIRIS-NG and ABI MESO data over the ray-matching sites. The ABI MESO data were sampled into the 5-deg ray-matching region. The ABI and AVIRIS-NG measurements have significantly different spatial resolutions. In general, the AVIRIS-NG data capture the fine features within the 5-deg ray-matching region. The ABI data show more averaged features, which matches the pattern in the AVIRIS-NG measurement. In each matched region, there are about 30, 120, and 30 pixels for ABI CH01, CH02, and CH03, respectively. This corresponds to covering ~0.8% of the ABI detector array over each ray-matching site. Over the eight ray-matched RoIs, the total number of detectors being evaluated is about 6.4% of the entire detector array for each ABI RSB channel. The uniformity analysis of ABI visible near-infrared (VNIR) detectors, e.g., with NSS data in Sec. 4, suggests that the radiometric biases of the fractional amount of ABI detector array can be used to characterize the overall radiometric biases of ABI VNIR channels.

To quantitatively evaluate the radiometric difference between ABI RSB and AVIRIS-NG measurements, mean radiance is calculated by averaging the radiance of the pixels within the ray-matching region. The bottom panels in Figs. 5–7 show the time series of the mean radiance with the standard deviation (bottom left panel) over the eight ray-matching sites derived from ABI MESO and AVIRIS-NG measurements and their percent differences with the error bar

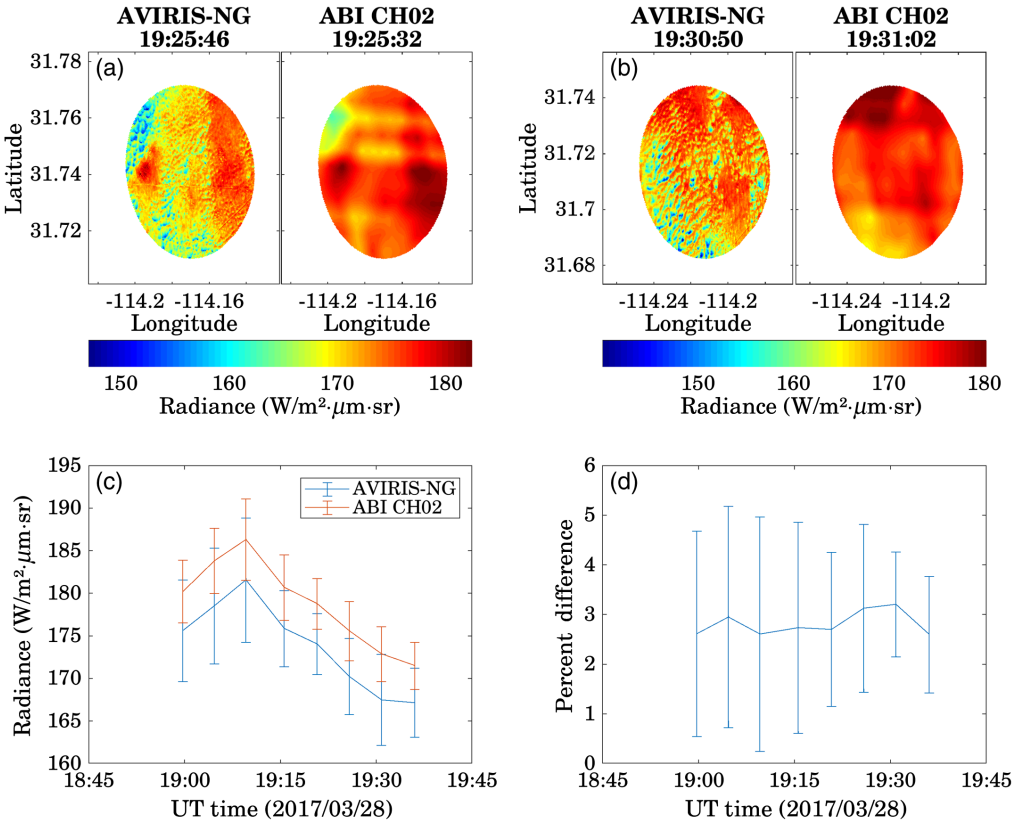

Fig. 6 Comparison of measured radiance between GOES-16 ABI and AVIRIS-NG for ABI CH02 during March 28, 2017. The arrangement of panels in this figure is similar to that in Fig. 5. (a) and (b) Comparison between sampled GOES-16 ABI MESO and AVIRIS-NG data over two ray-matching sites. (c) Mean radiance and standard deviation over the eight ray-matching sites (sequentially over time) were derived from GOES-16 ABI and AVIRIS-NG measurements for ABI CH02. (d) Time series of percent difference and error bar between the mean radiances of ABI and AVIRIS-NG over the ray-matching sites for ABI CH02. The ABI radiance over the ray-matching sites is consistently higher than that of AVIRIS-NG for ABI CH02.

(bottom right panel) for ABI CH01 to CH03. In general, the mean radiance of ABI CH01 and CH03, shown in the bottom panels of Figs. 5–7, matches that of AVIRIS-NG data closely over the eight ray-matching locations covering a wide range of radiance values. Over all of the eight ray-matching sites, the mean radiance of ABI CH02 is consistently higher than that of AVIRIS-NG. The ABI CH04 is a water vapor absorption band, and its measurement can be largely affected by the absorption due to the moisture content above the ER-2 aircraft. Therefore, the radiance difference between ABI and AVIRIS-NG for ABI CH04 is large and is not evaluated in this paper.

To further quantitatively evaluate the radiometric biases of five GOES-16 ABI RSB channels w.r.t. AVIRIS-NG measurements, we combined all of the paired radiance data observed by ABI and AVIRIS-NG over the eight ray-matched sites into the scatter plots as shown in Fig. 8. The AVIRIS-NG data were sampled onto ABI pixels satisfying the ray-matching condition for the pairing. The resulting mean biases [(ABI-AVIRIS-NG)/AVIRIS-NG, %] and uncertainty ($k = 1$, %) from the ABI versus AVIRIS-NG comparison are summarized in Table 2. In Table 2, we also list the $k = 1$ uncertainty (%) of AVIRIS-NG measurements[21] with SI traceability to NIST via the FEL lamp, the uncertainty due to the atmosphere above the aircraft, and the uncertainty of mismatch and variability. The total combined uncertainty (%) listed in Table 2 includes all three uncertainties, which makes the ABI measurement uncertainty SI traceable to NIST.

In addition, the linear regression fitting between the matched GOES-16 ABI MESO scene and AVIRIS-NG measurements are calculated and shown in Fig. 8 as red lines to evaluate the linearity of ABI measurements over the dynamic range limited by the ray-matched land scenes

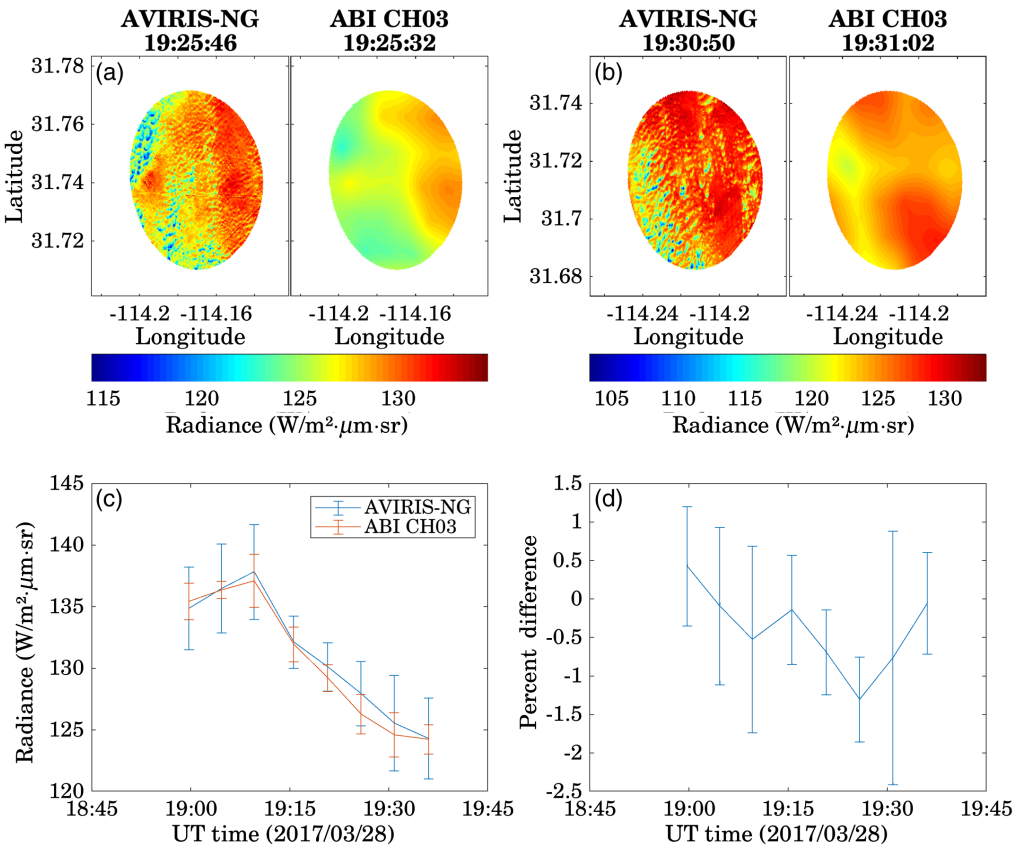

Fig. 7 (a)–(d) Comparison of measured radiance between ABI and AVIRIS-NG for ABI CH03 during March 28, 2017. The arrangement of panels in this figure is similar to that in Fig. 5.

during the field campaign. The correlation coefficients and root-mean-square-error (RMSE) of linear fitting between GOES-16 ABI and AVIRIS-NG measurements for the five ABI RSB channels are shown in Table 2. In general, the ABI CH03, CH05, and CH06 have better linearity than CH01 and Ch02 with linear correlation coefficients ≥ 0.95 when correlated with AVIRIS-NG measurements.

The radiometric biases of ABI CH01, CH03, and CH06 are <1% with the total uncertainty <2.5%. ABI CH02 and CH05 have positive radiometric biases, and ABI CH06 has negative biases. From Table 2, the radiometric biases $\pm$ uncertainties for all five ABI RSB channels are within the 5% radiometric accuracy requirement.

In Ref. 17, the NSS data that were collected during the ABI field campaign on March 28, 2017, were analyzed. Matched collocations between AVIRIS-NG and ABI NSS data collection on March 28, 2017, were identified for radiance comparison. The mean radiometric biases for ABI CH01, Ch03, and CH06 determined from NSS data were also shown to be within 2%, which is consistent with our evaluation. The magnitude of radiometric biases for these channels from our evaluation with ABI MESO data is also consistent with the independent analyses from the GEO-LEO collocation comparison between GOES-16 ABI and SNPP/NOAA-20 visible infrared imaging radiometer suite (VIIRS) RSB measurements[4,29–32] and GOES-16 ABI versus *in-situ* measurements in Ref. 33.

For ABI CH02, our analysis shows a mean positive bias of 2.85% $\pm$ 2.15%. The analysis of ABI CH02 NSS data in Ref. 17 shows ~7% positive bias relative to AVIRIS-NG. The magnitude of radiometric bias for ABI CH02 from NSS data analysis is closer to the ~6.4% radiometric bias determined from the independent analyses of the GEO-LEO, i.e., GOES-16 ABI versus SNPP VIIRS, collocation data comparison.[4,29–31] The relatively smaller bias determined from our MESO scene analysis for ABI CH02 in comparison with that derived from the NSS data and in the GEO-LEO comparison can be due to several factors such as different observation altitudes and atmospheric scattering, anisotropic land surface reflectance, remnant finite line-of-sight

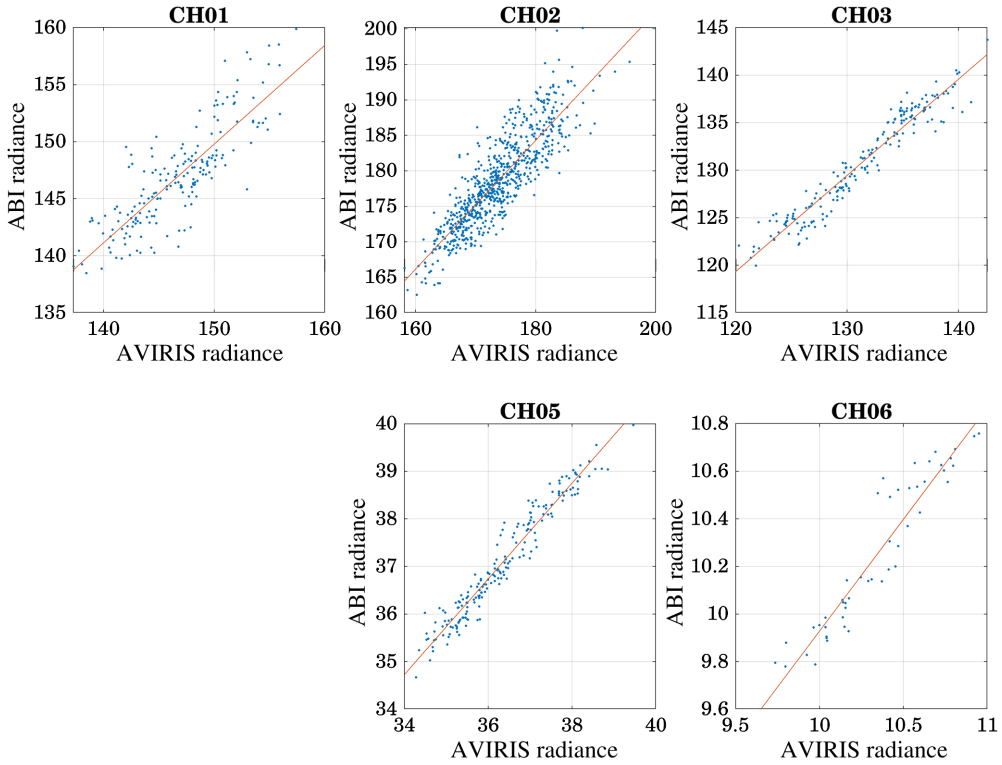

Fig. 8 Linear regression fit (red line) between matched GOES-16 ABI MESO scene and AVIRIS-NG measurements (blue scatter dots) for ABI RSB channels (CH01 to CH03, CH05, and CH06). Results were derived from the eight ray-matched field campaign measurements on March 28, 2017. AVIRIS-NG measurements were sampled onto ABI pixels satisfying the ray-matching condition.

Table 2 The mean bias (%), correlation coefficient, and RMSE of linear fitting between GOES-16 ABI and AVIRIS-NG measurements for five ABI RSB channels that are shown in Fig. 8. In addition, the ($k = 1$) uncertainties from ABI and AVIRIS-NG comparison, AVIRIS-NG measurements traceable to NIST via a FEL lamp,[21] atmosphere above aircraft, uncertainty of mismatch and variability, and total uncertainty (%) are also listed in the table.

ABI RSB channel	CH01	CH02	CH03	CH05	CH06
Mean bias (%) (GOES-16 ABI minus AVIRIS-NG)	0.18	2.85	-0.39	2.04	-0.88
Uncertainty of bias from GOES-16 ABI and AVIRIS-NG comparison ($k = 1$, %) (σ_{bias})	1.68	1.84	1.07	0.76	0.99
Uncertainty of AVIRIS-NG measurements ($k = 1$, %) ($\sigma_{\text{AVIRIS-NG}}$)	1.8	1.09	1.08	1.36	1.09
Uncertainty of mismatch and variability (σ_{mismatch})	0.03	0.14	0.24	0.16	0.28
Uncertainty of atmosphere ($k = 1$, %) (σ_{atmos})	0.11	0.15	0.00	0.01	0.01
Total uncertainty of GOES-16 ABI ($k = 1$, %) ($(\sigma_{\text{tot}} = \sqrt{\sigma^2_{\text{bias}} + \sigma^2_{\text{AVIRIS-NG}} + \sigma^2_{\text{mismatch}} + \sigma^2_{\text{atmos}}}$)	2.46	2.15	1.54	1.57	1.50
Correlation coefficient of GOES-16 ABI versus AVIRIS-NG comparison in Fig. 8	0.84	0.87	0.96	0.97	0.95
RMSE of linear fitting between GOES-16 ABI and AVIRIS-NG in Fig. 8 (W/m^2-sr-μm)	2.4	3.15	1.41	0.28	0.10

view angle differences, spectral characteristics difference, different footprint sizes, nonuniformity of ABI CH02 detector, and implementation of resampling to the ABI CH02 data. ABI CH02 has the smallest detector sizes compared with other ABI channels. Its resampling applies different weights to the 4×4 detector pixels around the fix-grid pixel to calculate grid radiance. From a close look at the top panels of Fig. 6, the fine distribution of AVIRIS-NG measurement over the 5-deg cone has a different detailed pattern in comparison with the averaged view by ABI. Although the line-of-sight view angle differences between ABI and AVIRIS-NG are confined to be within 5 deg, the field of view angles between ABI and AVIRIS-NG detectors are different. The difference in Fig. 6 can be due to the difference in the anisotropic scattering of fine ground features that AVIRIS-NG and ABI observe. In Sec. 4.2, the NSS data analysis indicates that the initial calibration of ABI CH02 results in large ($\pm 1.3\%$ in standard deviation) detector-to-detector nonuniformity. The observation of the Sonoran Desert with the ABI MESO scan covers a small subset of ABI detectors. The detector nonuniformity can also contribute to the ABI CH02 bias difference between our analysis and those in Refs. 17, 29–31.

The GOES-16 ABI RSB channel calibration relies on an onboard solar diffuser,[2] and the prelaunch characterization of the ABI solar diffuser reflectance model can directly affect the postlaunch radiometric performance of the ABI RSB channel. The possible cause of the particularly large bias ($\sim 6.4\%$) for GOES-16 ABI CH02 has been investigated and attributed to the error in the prelaunch solar diffuser bidirectional reflectance distribution function (BRDF) characterization for ABI CH02 (although alternative root causes continue to be investigated). The mitigation of the GOES-16 ABI CH02 bias was implemented using a rescaled solar diffuser BRDF table, i.e., K parameter table of the ABI solar diffuser, in solar calibration. The radiometric bias of GOES-16 ABI CH02 was reduced by $\sim 6.4\%$ on April 23, 2019, after the implementation of the new solar diffuser K parameter table.

3 Radiometric Comparison with S-HIS Measurements for GOES-16 ABI TEB Channels

3.1 *GOES-16 ABI TEB and S-HIS Measurement Collection and Processing*

The GOES-16 ABI has ten TEBs covering the spectral range from 3.9 to 13.3 μm (Table 3) with a spatial resolution of ~ 2 km. During the March to May GOES-16 ABI field campaign, data over night for the ocean target in the Gulf of Mexico were collected with S-HIS and analyzed in Refs. 17 and 27 to evaluate (by quantifying the bias) and validate (by comparing against requirements and results from other calibration methods) the GOES-16 ABI TEB performance. In particular, in Refs. 17 and 27, the ABI NSS data over the open ocean in the Gulf of Mexico were compared with S-HIS measurements collected during the field campaign flight conducted on April 13, 2017.

In this paper, we analyze the GOES-16 ABI TEB data from MESO scans of land collected under the ABI timeline 25 scheduling during the field campaign on March 28, 2017. The targeted field campaign location on March 28, 2017, is around the Sonoran Desert. Under the 5-min timeline 25 mode, there are ten MESO scans, and each ABI MESO scan consists of two swaths covering the targeted location for each of the ABI channels. Coordinated simultaneous air-borne measurements by S-HIS were performed for $\sim$90- min [from universal time (UT) 18:45 to UT 20:15] during the field campaign on March 28, 2017. Figures 9 and 10 show the trajectory of the S-HIS instrument on board the ER-2 aircraft and the scanning footprints of S-HIS on March 28, 2017. Because the ABI MESO scan mode is different from the ABI NSS mode, the surface characteristics (ocean versus land) and detector coverage in the analysis of Refs. 17 and 27 are

Table 3 ABI TEB channel wavelengths.

ABI TEB channel	7	8	9	10	11	12	13	14	15	16
Wavelength (μm)	3.9	6.2	6.9	7.3	8.4	9.6	10.3	11.2	12.3	13.3

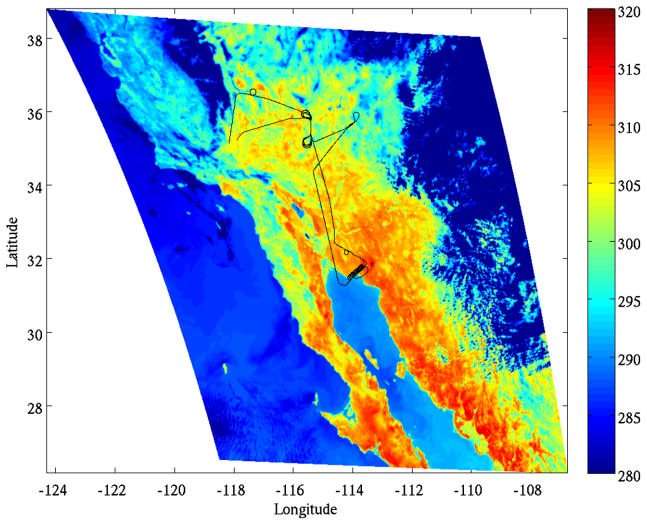

Fig. 9 Trajectory of ER-2 (black line) overlaid on GOES-16 CH14 BT image during the field campaign on March 28, 2017.

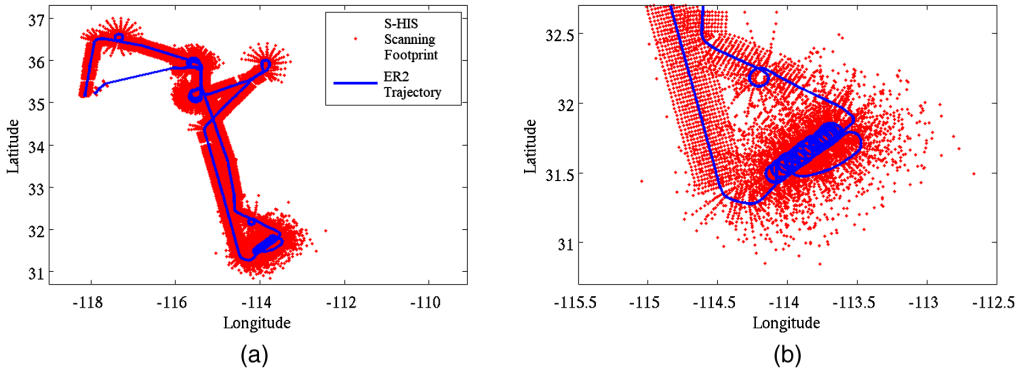

Fig. 10 Trajectory (blue line) of S-HIS instrument on board the ER2 aircraft and the surface location of the scanning footprints of S-HIS (red dots) during the field campaign on March 28, 2017. (a) overall trajectory and (b) zoom in view over the Sonoran Desert region.

different from those analyzed in this paper. But the general ray-matching methodology used in Ref. 17 for selecting data is similar to what we used in this paper.

The S-HIS is an FTS[23–26] that measures thermal radiation at high-spectral resolution, scanning the Earth in swaths up to 40-km wide to collect data on temperature and water vapor. The basic components of the S-HIS include a scene mirror module, telescope, Michelson plane mirror interferometer, aft optics, detector module with mechanical cooler, laser metrology, calibration blackbodies, and on-board signal processing and solid-state storage. The spectral coverage of S-HIS spans from 3.33 to 17.24 μm (4607 channels) with a spectral resolution of 0.48 1/cm. The S-HIS was calibrated prelaunch with the radiometric uncertainty of ~0.04 k, which has SI traceability to the NIST TXR radiometer. The NIST TXR validation of the S-HIS uncertainties over the temperature range 227 to 290 K was discussed in Ref. 26. The impacts of the changing environment are handled in a variety of ways as detailed in Ref. 24.

The S-HIS has a 100-μrad spatial field of view, producing 2-km diameter nadir footprints from an altitude of 20 km. The S-HIS observes Earth and internal calibration bodies by rotation of the scan mirror. During each cross-track scan, the scan mirror sequentially takes 14 views of Earth and can scan as far as 40 deg off-nadir, which can match the ABI view geometry over the target location. On March 28, 2017, about eight circular flight trajectories were carried out over the region of the Sonoran Desert.

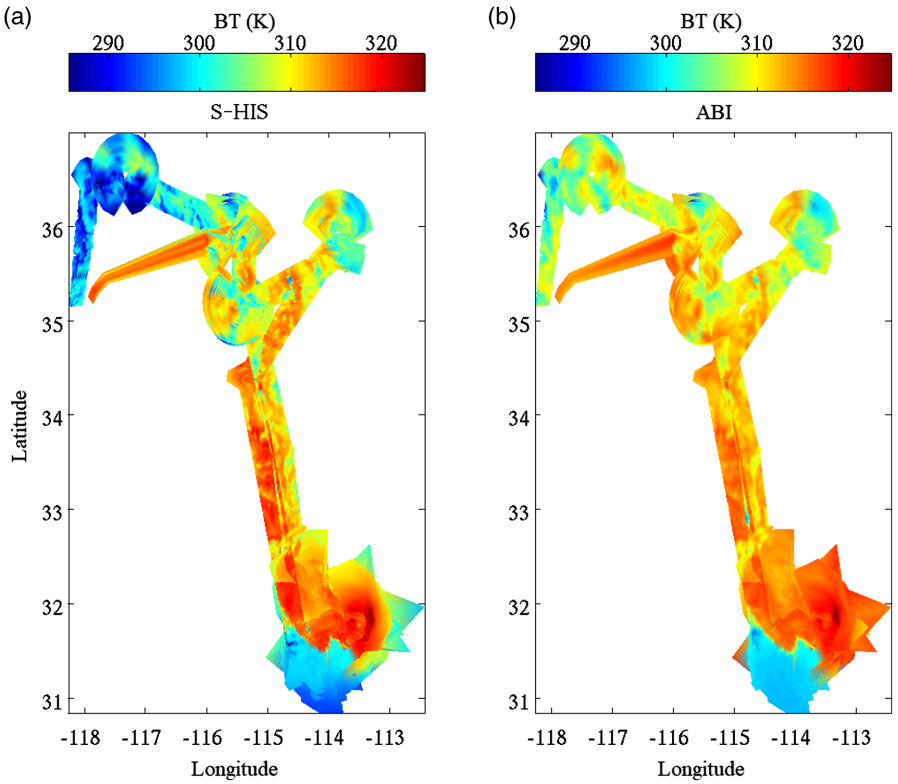

Fig. 11 (a) BT map derived from S-HIS data and (b) sampled GOES-16 ABI data for ABI CH14. The data were collected on March 28, 2017.

The special scan data of GOES-16 ABI TEB data collected during the field campaign were also calibrated and navigated by the GOES-16 ABI vendor, i.e., the Pleiades version. In the Pleiades version of reprocessed ABI TEB data, the calibration with an onboard blackbody to derive the detector gain factor, the processing of the raw detector counts to radiance data and the image navigation were all performed by the ABI vendor. Figure 11 shows an example of the BT map derived from S-HIS data [Fig. 11(a)] and ABI data [Fig. 11(b)] for ABI CH14 on March 28, 2017. The ABI MESO scan data were resampled onto the S-HIS scanning footprint for comparison. The S-HIS hyperspectral data were convolved with the SRF of ABI CH14. The BT maps derived from S-HIS and ABI measurements are consistent. The difference between the two panels is mainly due to different sensor view angles and data collection frequencies.

3.2 *ABI and S-HIS BT Comparison Results*

To determine the BT bias between GOES-16 ABI and S-HIS measurements for a given ABI TEB channel, identifying optimally matched view geometry samples in time and space between GOES-16 ABI and the airborne reference S-HIS sensor is required. A similar ray-matching condition used in Sec. 2, e.g., the view-angle difference between the ABI and S-HIS line of sights within 5-deg and temporal matching within 30 s, was applied in searching for the qualified matching locations. Due to the scanning geometry difference between AVIRIS-NG and S-HIS, the resulting ray-matched locations are different.

Because S-HIS can scan as far as 40 deg off-nadir, it is easy to match the ABI view geometry over the target location during the circular flight paths of the ER-2 aircraft on March 28, 2017. Figure 12 shows the 11 scanning locations of S-HIS around the Sonoran Desert region that satisfy the ray-matching condition. These matched locations were all over land. The ABI MESO mode scans through the region every 30 s, and the time stamps of S-HIS data over the RoIs are used to find the closest ABI MESO data in time. Figure 13 shows an example of spectral BT from S-HIS (black line) and BT of 10 ABI TEBs (colored thick horizontal lines) over one ray-matched RoI. In general, the BTs of ABI TEBs are well aligned with the spectral BT from S-HIS.

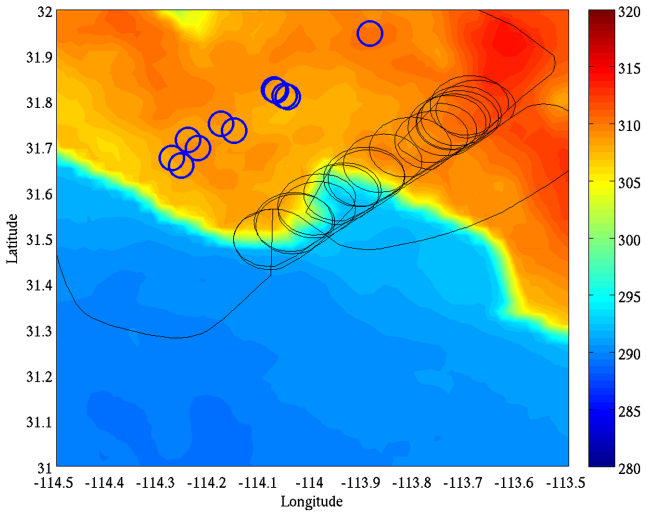

Fig. 12 The selected ray-matching sites (blue circles) between ABI and S-HIS overlaid onto the BT map of ABI CH14 MESO scene. The black line is the trajectory of S-HIS during the field campaign on March 28, 2017.

The S-HIS spectral radiance data are further convolved with the ABI SRFs, and the resulting BTs derived from S-HIS for the corresponding ABI TEBs are compared with the GOES-16 ABI BT measurements for BT bias evaluation. Table 4 and Fig. 14 summarize the BT bias (ABI minus S-HIS) and uncertainties ($k = 1$) from the comparison between ABI MESO data and S-HIS field campaign data collected over the Sonoran Desert region on March 28, 2017. The BT bias value was converted to a 300 K BT scene equivalent by converting the radiance difference to the equivalent BT bias at 300 K. In Table 4, the uncertainty of the S-HIS measurement row shows the ($k = 1$) uncertainty traceable to NIST TXR. The NIST TXR validation of the S-HIS measurement uncertainties over the temperature range 227 to 290 K was discussed in Ref. 26. The total uncertainty row shows the combined uncertainties of ABI TEB measurement traceable to NIST TXR using S-HIS as the transfer sensor. The propagation of individual uncertainty contribution to the total uncertainty is calculated in radiance percent. The total uncertainty (K) at the 300 K scene equivalent in the last row of Table 4 is converted from the total uncertainty in radiance percent.

Table 4 ABI TEB biases (K) and $k = 1$ total uncertainty (K) at the 300 K scene equivalent derived from the ABI versus the S-HIS comparison. The ($k = 1$) uncertainty (radiance %) from the ABI and S-HIS comparison, uncertainty of S-HIS measurements traceable to NIST TXR,[26] uncertainty of atmosphere and total uncertainty (%) are also listed in the table. The total uncertainties at the 300 K scene equivalent in last row are converted from the total uncertainty in radiance percent.

ABI TEB channel	7	8	9	10	11	13	14	15	16
Bias (K)	0.97	0.09	0.20	0.10	0.55	−0.42	−0.42	−0.08	−1.02
Uncertainty ($k = 1$) (radiance %) of bias from comparison (σ_{bias})	2.74	0.31	0.37	0.66	0.61	0.41	0.32	0.37	0.61
Uncertainty of S-HIS measurement (radiance %) ($\sigma_{S-\text{HIS}}$)	0.12	0.13	0.12	0.11	0.09	0.08	0.07	0.07	0.06
Uncertainty of atmosphere (radiance %) σ_{atmos}	0.06	0.16	0.2	0.16	0.05	0.05	0.02	0.03	0.11
Total uncertainty (radiance, %) ($\sigma_{\text{tot}} = \sqrt{\sigma_{\text{bias}}^2 + \sigma_{S-\text{HIS}}^2 + \sigma_{\text{atmos}}^2}$)	2.74	0.37	0.43	0.68	0.61	0.42	0.33	0.38	0.62
Total uncertainty (K) at 300 K	0.66	0.14	0.29	0.32	0.33	0.27	0.23	0.29	0.51

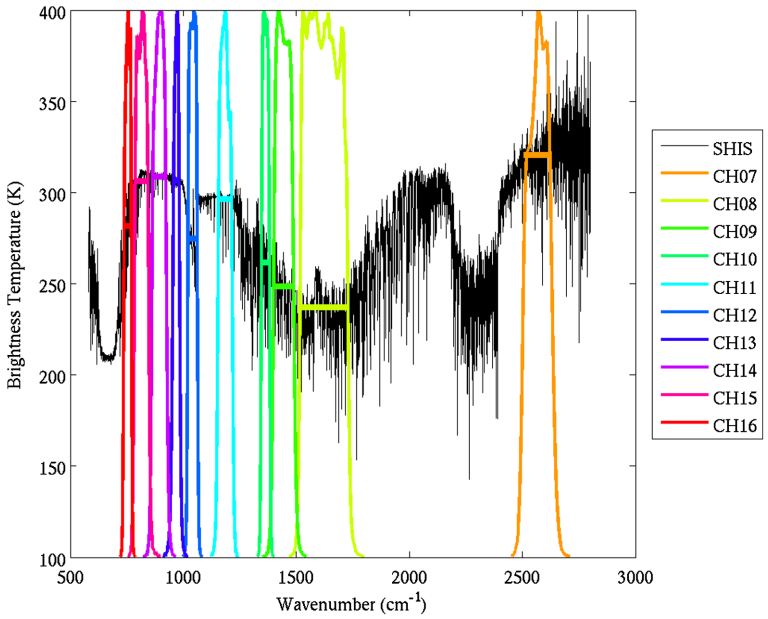

Fig. 13 Example of spectral BT from S-HIS (black line) and BTs of 10 TEBs measured by GOES-16 ABI (colored thick horizontal lines) over a ray-matching site between ABI and S-HIS. The SRF for the 10 ABI TEBS (color lines) is overlaid for illustration.

From Fig. 14 and Table 4, the ABI CH08 to CH10 has a positive mean BT bias, all being <0.20 K with uncertainty <0.35 K. The BT bias of ABI CH11 is $\sim 0.55 \pm 0.33$ K. The ABI CH13 to CH15 has a negative BT bias with the amplitude being <0.45 K and uncertainty <0.3 K. The ABI CH16 has a negative BT bias -1.02 ± 0.51 K due to the CO_2 absorption above the ER-2 aircraft. From Table 4, the radiometric biases $\pm$ uncertainties for ABI TEB channels CH08 to CH11 and CH13 to CH15 are all within the 1 K radiometric accuracy requirement.

There were independent evaluations of the radiometric bias of GOES-16 ABI TEBs in Ref. 27 using the MESO and NSS data over ocean collected during the ABI field campaign on April 13, 2017. The BT biases determined from NSS and MESO data over ocean in Ref. 27 show that the BT bias for ABI CH08 to CH11 are all positive and <0.5 K, and the biases for CH13 to CH15 are all negative with a magnitude within 0.4 K. The overall BT biases of ABI CH08 to CH11 and CH13 to CH15 determined from land scenes in this paper are consistent in both sign and magnitude with those determined from the measurements over ocean on April 13, 2017, in Ref. 27. The biases of ABI CH08 to CH11 and CH13 to 15 being <0.5 K are also consistent with TEB bias evaluation results from the GEO-LEO comparison between GOES-16 TEB and hyperspectral infrared measurement by the cross-track infrared sounder (CrIS) on board the SNPP satellite.[34]

For ABI CH07 (3.9-μm channel), the BT bias over land is 0.97 ± 0.66 K as determined in this paper whereas the bias determined from the ocean scene in Ref. 27 is 0.24 K, both of which are positively biased but with different magnitudes. The difference in ABI CH07 bias over different surface types can be due to the ABI 3.9-μm channel observing both thermal emission and reflected solar radiation (Fig. 15). The land surface has a larger spatial variability in surface temperature and emissivity in comparison with ocean. In addition, the influence of reflected solar radiation over land is also larger than over ocean. As discussed in radiometric and spectral validation of atmospheric infrared sounder (AIRS) observations with the S-HIS,[25] the S-HIS and AIRS have different observation altitudes, footprint sizes, and spectral characteristics. These differences are also applicable here when comparing S-HIS and ABI. Overland, the surface emissivity and reflectance variations for ABI CH07 are more significant and more anisotropic than over ocean. During the scanning of ray-matched land pixels, the ABI detectors over land are at a higher altitude than S-HIS and might observe more scattered radiation from the nearby land surfaces while transmitting through the atmosphere than those over the ocean, which makes ABI CH07 appear to have a larger BT bias than over ocean.

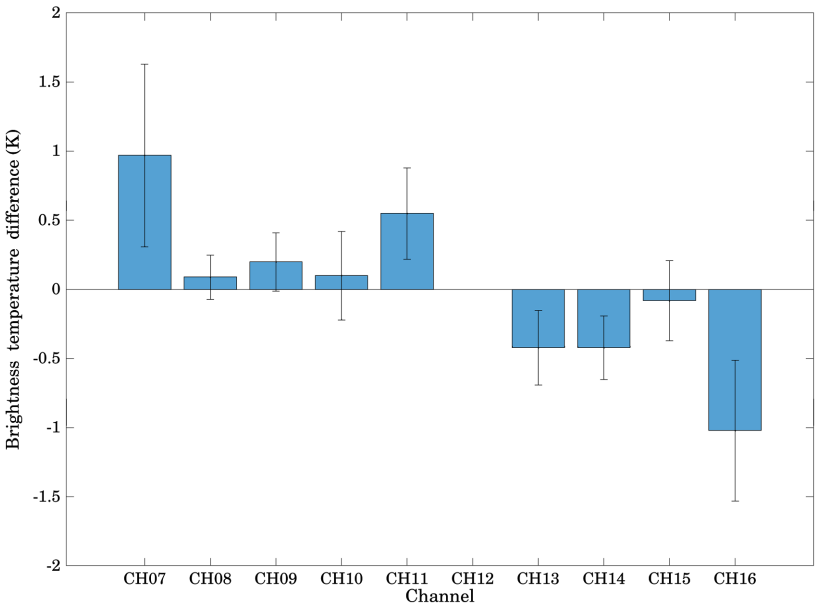

Fig. 14 GOES-16 ABI and S-HIS BT difference (ABI minus S-HIS) and ($k = 1$) total uncertainty derived from the March 28, 2017, MESO data comparison. The BT bias value and uncertainty were converted to the 300 K BT scene equivalent.

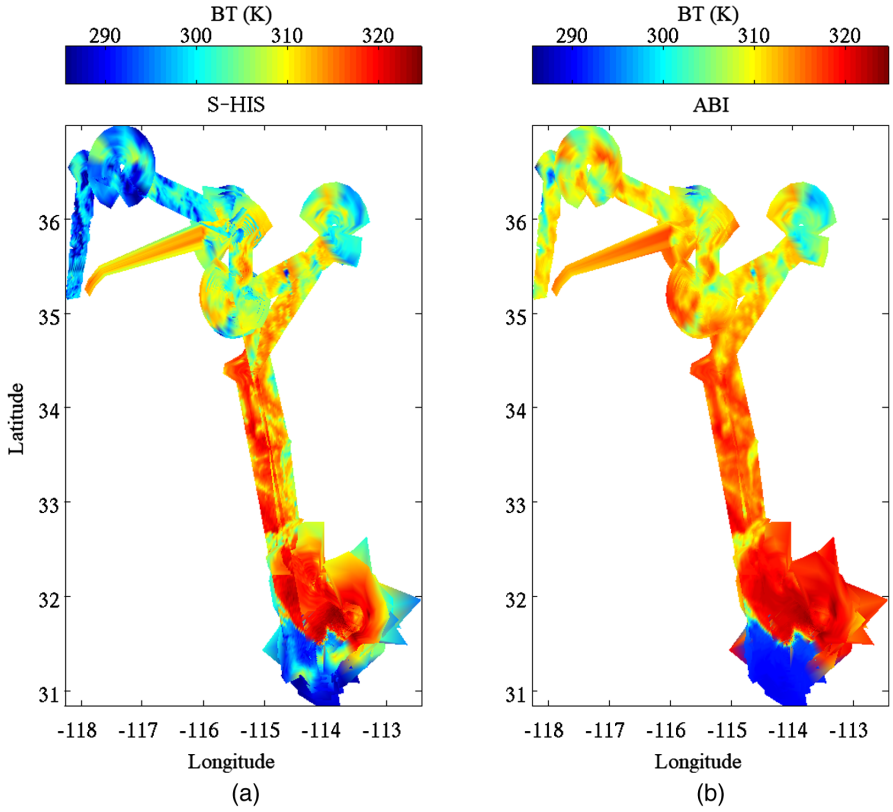

Fig. 15 Comparison of BT maps derived from (a) S-HIS data and (b) GOES-16 ABI data processed by Pleiades for ABI CH07. The data were collected on March 28, 2017.

The ABI CH12 (9.6 μm) and CH16 (13.3 μm) are the ozone and CO_2 absorption channel, respectively, as shown in Fig. 13. The absorption by the cold atmosphere above ER-2 can cause ABI CH12 and CH16 to have a negative BT bias. In particular, for CH12, the (ABI minus S-HIS) bias can be > -10 K due to stratospheric O_3 absorption. For these two channels, radiative

transfer modeling (RTM) corrections are needed to account for the atmosphere above the aircraft to reconcile the BT bias between GOES-16 ABI and S-HIS measurements.

4 Reanalysis of NSS Data for GOES-16 ABI RSB Detector Uniformity Evaluation

The ABI uses large focal plane arrays with detector numbers varying from 372 for CH04 and CH06 to 1460 for CH02 as listed in Table 1. It is a challenge to ensure the radiometric uniformity among such a large number of detectors for both the RSB and TEB channels of ABI. There were several implementations and updates of the ABI solar calibrations, which resulted in different versions of detector gains and nonlinear calibration factors and consequently different detector uniformity performance. The NSS data collected during special scans of ABI provide unique ways to quantitatively evaluate the quality of detector uniformity.

During the timeline 25 mode of ABI, NSS was also performed. The ABI NSS was performed by fixing the ABI east/west scan mirror angle while rotating the ABI NSS mirror. The NSS mode is designed to make the detector of each ABI channel sequentially scan through the same location over the target region and to evaluate the detector uniformity for each ABI channel. Because the detector array of different ABI channels is located at different locations on the focal plane module of ABI, during each NSS, only the detector array of the selected channel can scan through the targeted location while the detectors of all other channels are away from the target location. Therefore, under the ABI timeline 25 mode, the NSS is designed to scan over the target location when the ABI swath number = channel number. As the ABI swath number varies, the target location is scanned sequentially by different ABI channels. During the 5-min ABI timeline 25 mode, the NSS was repeated four times for each ABI channel.

In this section, we perform reanalysis of the NSS data collected during the GOES-16 ABI field campaign on March 28, 2017, and lunar scans on April 10, 2017, using two versions of calibration algorithms to demonstrate the effectiveness of ABI NSS in evaluating the improvements in ABI RSB detector uniformity performance.

4.1 *Calibration and Calculation of ABI RSB Radiance Data*

The radiance observed by the GOES-16 ABI RSB channel viewing the Earth scene is determined from the measured counts (C) of the Earth view (ev) and the space view (sv) as follows:

$$\langle L_{\mathrm{ev}} \rangle = \frac{M\Delta C_{\mathrm{ev}} + Q\Delta C_{\mathrm{ev}}^2}{\rho_{\mathrm{NS}}^{\mathrm{ev}} \rho_{\mathrm{EW}}^{\mathrm{ev}}}, \tag{1}$$

where $\langle L_{\mathrm{ev}} \rangle$ is the band-averaged spectral radiance ($\mathrm{W/m^2\text{-}sr\text{-}\mu m}$) for the scene in the ABI Earth view. ΔC_{ev} is the count difference between the Earth view and space view, i.e., $\Delta C_{\mathrm{ev}} = C_{\mathrm{ev}} - C_{\mathrm{sv}}$. The $\rho_{\mathrm{NS}}^{\mathrm{ev}}$ and $\rho_{\mathrm{EW}}^{\mathrm{ev}}$ are the reflectance of the east/west and north/south scan mirrors, respectively, when viewing the targeted scene. M and Q are the linear and quadratic coefficients, respectively. The quadratic coefficient Q is first determined prelaunch per band and per detector element and later is updated during postlaunch. The linear coefficient M for ABI RSBs is determined in on-orbit viewing of the solar calibration target (SCT), which is a solar diffuser. Here, we summarize the onboard calibration of ABI RSBs using the solar diffuser. Details about ABI solar calibration can be found in Refs. 4 and 5. The SCT-based calibration of ABI RSBs was carried out biweekly to monthly in 2018 by determining the linear calibration coefficient M for each of the detectors in ABI RSBs. During the solar calibration (around UT 11:00 for GOES-16 ABI), the solar diffuser port is open to allow the solar light to shine on the solar diffuser. The east/west and north/south scan mirrors will be oriented to let the ABI detector array observe the scattered light from the solar diffuser. When viewing the SCT, the scattered solar radiance observed by a particular detector in the ABI detector array of a given RSB channel is calculated through the following equation:

$$\langle L_{\mathrm{SCT}} \rangle = K_{\beta_{\mathrm{eff}}}^{\text{detector row\#}} \cos(\theta_{\mathrm{Sun}}) \frac{\Phi_{\mathrm{Sun}}}{4\pi d_{\mathrm{ES}}^2}, \tag{2}$$

where the factor $K_{\beta_{\mathrm{eff}}}^{\text{detector row\#}}$ is related to the effective channel-dependent BRDF of the SCT, which is the instrument property parameter and is determined prelaunch as a function of solar azimuthal angle (β_{eff}) and detector rows. The θ_{Sun} is the solar zenith angle w.r.t. the solar diffuser panel normal. Φ_{Sun} is band-averaged solar irradiance. The d_{ES} is the Sun–Earth distance normalized by mean Sun–Earth distance, i.e., one astronomical unit (AU). The actual observed count difference between SCT view and space view, i.e., $\Delta C_{\mathrm{SCT}} = C_{\mathrm{SCT}} - C_{\mathrm{sv}}$, by a particular ABI detector is related to the observed SCT view radiance $\langle L_{\mathrm{SCT}} \rangle$ [Eq. (2)] through the following calibration equation:

$$\langle L_{\mathrm{SCT}} \rangle = \frac{M \frac{\Delta C_{\mathrm{SCT}}}{f_{\mathrm{int,ch}}} + \frac{f_Q}{f_{\mathrm{int,ch}}} Q \Delta C_{\mathrm{SCT}}^2}{\rho_N^{\mathrm{SCT}} \rho_E^{\mathrm{SCT}}}, \tag{3}$$

where $f_{\mathrm{int,ch}} = 9$ and accounts for the nine-time longer integration time when viewing the SCT than observing the Earth scene. f_Q is a factor needed to account for impacts of integration time difference and was initially set as 1 and later was updated for ABI calibration in early 2018. We will discuss the change of f_Q in a later part of this section when we introduce the updated calibration algorithm. In Eq. (2), the $\rho_{\mathrm{NS}}^{\mathrm{SCT}}$ and $\rho_{\mathrm{EW}}^{\mathrm{SCT}}$ are the reflectance of the east/west and north/south scan mirrors, respectively, when viewing the SCT. From Eq. (3) together with $\langle L_{\mathrm{SCT}} \rangle$ calculated from Eq. (2), we calculate the linear gain factor M for each of the ABI RSB detectors using following equation:

$$M = \frac{f_{\mathrm{int,ch}} \langle L_{\mathrm{SCT}} \rangle \rho_N^{\mathrm{SCT}} \rho_E^{\mathrm{SCT}} - f_Q Q \Delta C_{\mathrm{SCT}}^2}{\Delta C_{\mathrm{SCT}}}. \tag{4}$$

The linear calibration coefficients, i.e., M look-up-table (LUT), for each ABI RSBs are updated as needed in operational ABI level-1B data production after the ABI solar calibration is completed.

From March to May of 2017, when the GOES-16 ABI NSS data used in this paper were collected, there were various postlaunch tests being performed to support the radiometric and geolocation calibration of GOES-16 ABI and its performance evaluation. Over the lifetime of GOES-16, the operational calibration of ABI RSBs experienced several updates of calibration parameters such as the best detector selection (BDS) LUT, nonlinear calibration factor, solar diffuser BRDF LUT, and integration factor in solar calibration. These developments and updates in the calibration algorithm helped to improve the radiometric quality of ABI RSB images. The updated calibration algorithms result in different versions of detector gain (M) and nonlinear calibration factor (Q) LUT. In this section, the solar calibration model used is the in-house version developed at the NOAA Center for Satellite Applications and Research (STAR), which enables the flexibility of evaluating the radiometric performance of different solar calibration algorithms.

In this paper, the NSS data of GOES-16 ABI CH01 to CH03 from field campaign and lunar scans are reprocessed using the following two versions of detector linear (M) and nonlinear calibration factor (Q).

4.1.1 *Original calibration algorithm (version O)*

This version of solar calibration uses the prelaunch nonlinear calibration factor Q LUT in the solar calibration to derive the detector gain factor (M). Full nonlinear calibration factor (Q) without scaling, i.e., $f_Q = 1$ in Eqs. (2) and (4), is used in solar calibration. Equation (1) is used in converting the background-subtracted raw count data to radiance data. As shown in Table 5, the calibration coefficients and scheme used before January 17, 2018, in the operational level-1B GOES-16 ABI data production is referred to as the version O calibration algorithm.

Table 5 Operational solar calibration updates for GOES-16 ABI in early 2018.

Date	Calibration update	Affected ABI bands
Before January 17, 2018 (original calibration algorithm)	$f_Q = 1$	CH01, CH02, CH03, CH04, CH05, and Ch06
January 17, 2018, to February 17, 2018	Update Q LUT to new Q_n LUT	CH01, CH02, and CH03
After February 07, 2018 (updated calibration algorithm)	$f_Q = 1/f_{\text{int,ch}} = 1/9$ (with Q-scaling)	CH01, CH02, CH03, CH04, CH05, and CH06

4.1.2 *Updated calibration algorithm (version U)*

The Q-scaling scheme and updated Q LUT are implemented in solar calibration. During the solar diffuser calibration event for ABI RSB, the reflected solar light from the solar diffuser is weak due to the partial aperture structure of ABI; the integration time during the solar diffuser view was set to be nine times that of the integration time of the Earth view. Therefore, ΔC_{SCT} is nine times larger than the equivalent Earth view. On the other hand, the Q factor was derived during prelaunch with a normal integration time. From Eq. (2), it can be seen that the factor $f_{\text{int,ch}}$ can only account for scaling down ΔC_{SCT} linearly, and the quadratic term ΔC_{SCT}^2 associated with Q requires additional scaling. When setting $f_Q = 1$ in Eqs. (2) and (4) used for the original ABI calibration algorithm, it was suggested that the striping in the ABI RSB images might be due to the amplified effect of the nonlinear Q factor in the solar calibration.

Therefore, the Q-scaling scheme was implemented to scale the nonlinear Q factor down by the corresponding integration time factor for the solar diffuser view, i.e., nine and consequently $f_Q = 1/9$ in Eqs. (2) and (4), in the solar calibration to derive the linear detector gain factor M. This update is the so-called Q-scaling scheme and was applied to all ABI RSB channels (CH01 to CH06). When applying the derived linear gain factor M into Eq. (1) to calculate the Earth view radiance, full-Q without scaling was used in converting the background-subtracted raw Earth view count data to radiance data. For ABI CH01 to CH03, the striping is still significant after the Q-scaling update, and it is due to the change in the detector nonlinear response after the satellite launch. In early 2018, new nonlinear Q LUT was developed together with the Q-scaling scheme by the ABI ground system (GS)/vendor to mitigate the striping problem for ABI CH01, CH02, and CH03. The timeline of implementations of Q-scaling calibration scheme for all ABI RSB channels and updating of Q calibration coefficients for ABI CH01 to CH03 is documented in Table 5. As shown in Table 5, the calibration coefficients and algorithm implemented after February 07, 2018, in the operational level-1B GOES-16 ABI data production is referred to as the version U calibration algorithm in this paper. In the version U calibration algorithm, the linear detector gain factor M was derived from Eq. (4) by implementing both the Q-Scaling scheme and the updated Q LUT, i.e., Q_n LUT, for ABI CH01 to CH03.

The update of the calibration scheme from version O to version U provides good testing cases to benchmark the variation of detector uniformity due to changes in the ABI RSB radiometric calibration algorithm. In the following sections, the reanalysis of NSS data uses the calibration coefficients derived from the March 16, 2017, solar diffuser observation. Both the NSS data of GOES-16 ABI CH01 to CH03 from the field campaign and lunar scans are reprocessed using detector linear (M) and nonlinear calibration factor (Q) derived from the version O and U solar calibration, respectively. In doing so, the raw count data of NSS collection were reprocessed to radiance data according to Eq. (1) for the given pair of linear and nonlinear calibration factor LUTs.

4.2 *Detector Uniformity Evaluation Through Reanalysis of ABI NSS Data from Field Campaign*

4.2.1 *ABI NSS data collection during field campaign*

The ABI NSS data collection during the field campaign on March 28, 2017, was executed under timeline 25 scheduling. Figure 16 shows the sample ground track of ABI NSS during timeline 25 for CH01 around UT 19:25 on March 28, 2017. Figure 17 shows example of NSS data for

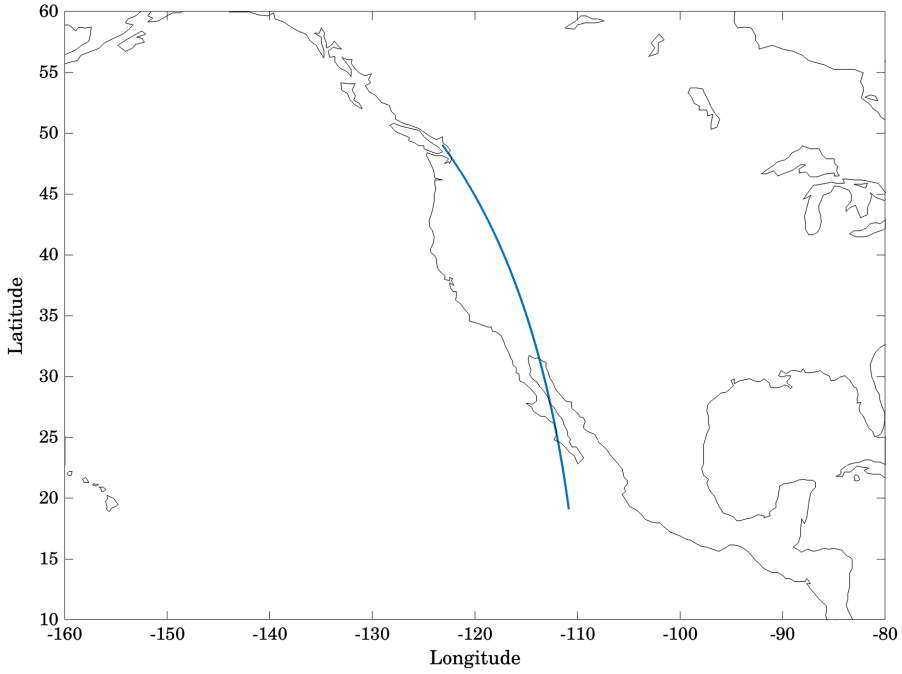

Fig. 16 Ground track of GOES-16 ABI NSS during timeline 25 for CH01 around UT 19:25 on March 28, 2017. The ABI NSS during timeline 25 is designed to overpass the target location for swath number = channel number.

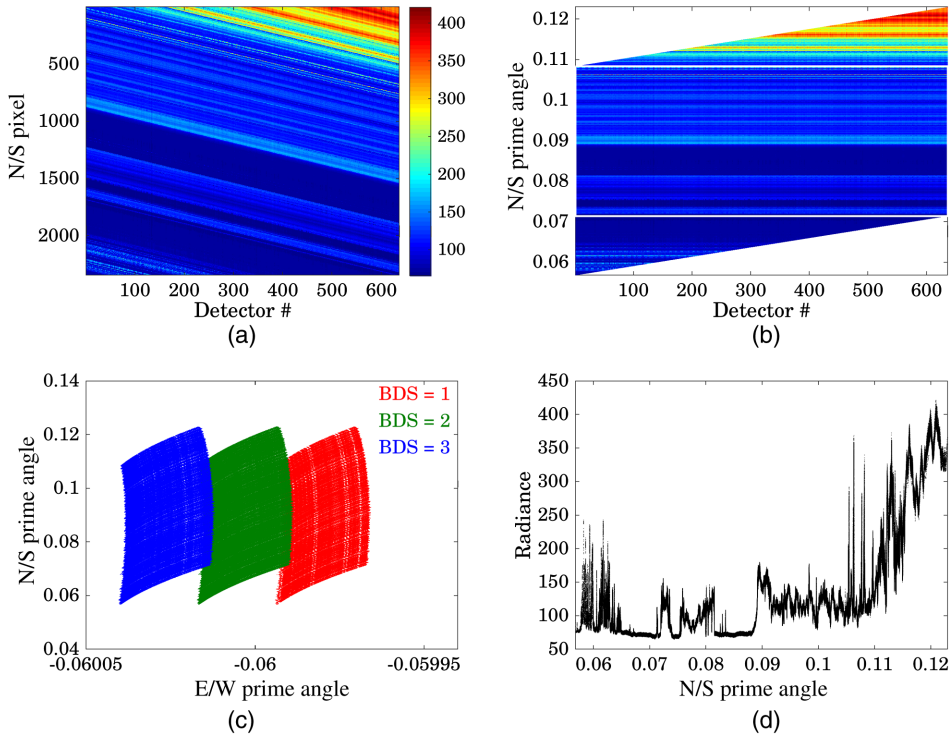

Fig. 17 (a) Pixel map of the ABI CH01 NSS radiance (W/m^2-sr-μm) data in detector-N/S pixel coordinate. (b) NSS data reorganized in the detector-N/S prime angle (radian) coordinate. The region for calculating detector-mean radiance $\overline{L_{c,k}}$ is marked as the white rectangle box. (c) The E/W and N/S scan angle (radian) locations for all of detectors of ABI CH01 during NSS. The color coding indicates the column number for these detectors. (d) All-detector-averaged radiance (W/m^2-sr-μm) versus N/S scan angle (radian), showing large variation of radiances corresponding to the variety of surface features during NSS.

ABI CH01. Figure 17(a) shows the measured radiance in the detector-N/S pixel coordinate, i.e., pixel map. The slanted stripe indicates the sequential scan of the same location by all of the detectors during NSS. It is difficult to directly extract data over the same region from the pixel map. Therefore, NSS data were reorganized in the coordinate of detector-N/S prime angle, i.e., the N/S scan angle of ABI [see Fig. 17(b)]. Such a coordinate transformation enables the detector-uniformity evaluation. To minimize the noise in the data and increase the sample size, the NSS data within 96% of the common N/S prime angle range for all of the detectors are collected.

Figure 17(c) shows the E/W and N/S scan angle locations for all of ABI CH01 detectors during NSS. The locations are color-coded with the ABI BDS identifier (column number). Because the detector array for each ABI channel has multiple columns, one best detector is selected for each row of ABI detectors, and the selected detector is labeled with the BDS identifier. For ABI CH01, there are three columns in the detector array with the BDS identifier ranging from 1 to 3. It can be seen that there are small differences in the E/W scan angle locations among the detectors with different BDS identifiers. The data within 96% of the common N/S prime angle range are averaged over the same N/S prime angle range for each detector, and the resulting mean radiance is labeled as $\overline{L_{c,k}}$ for detector k of column c, which is used to evaluate the detector uniformity.

4.2.2 *Detector uniformity evaluation with NSS data from field campaign*

In this section, the reanalysis results of ABI CH01 to CH03 NSS data are shown. Figure 18 shows the normalized mean-radiance among detectors derived from the reprocessed radiance data using the version O and U calibration models for ABI CH01 to CH03. After the mean-radiance $\overline{L_{c,k}}$ is calculated by averaging the detector radiance over the same N/S scan angle range, the normalized mean-radiance ($NL_{c,k}$) for detector k of column c is defined as

$$\mathrm{NL}_{c,k} = \frac{\overline{L_{c,k}}}{\overline{L_c}}, \tag{5}$$

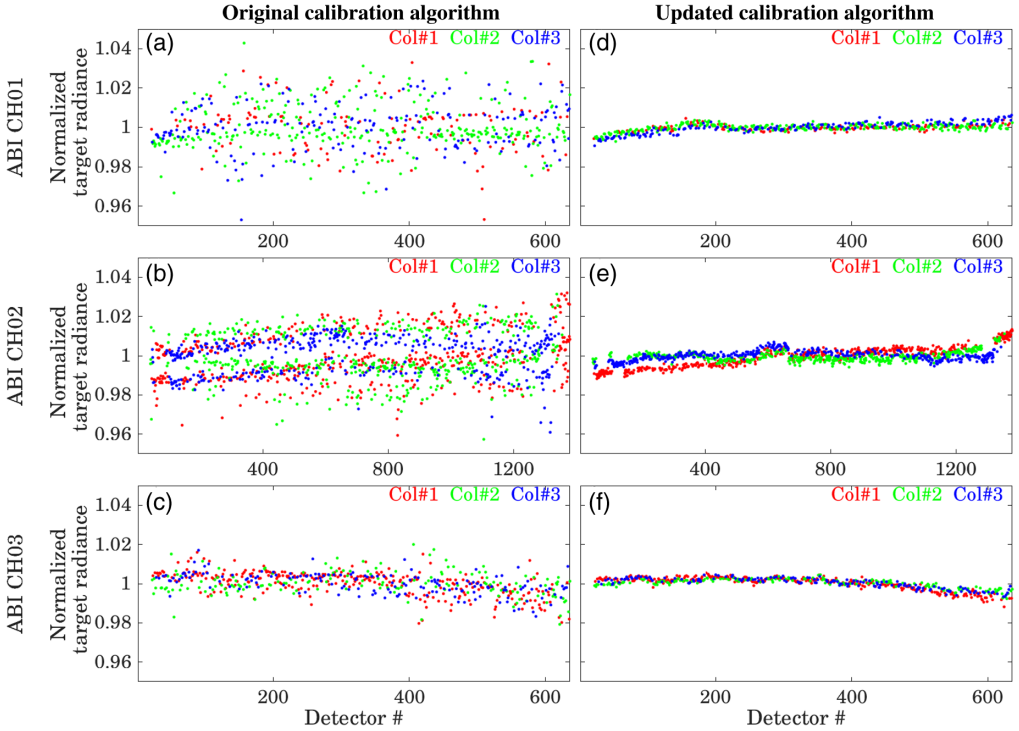

Fig. 18 Detector-uniformity analysis with normalized mean-radiance $NL_{c,k}$ (%) among detectors of column c ($c = 1$, 2, and 3) for ABI CH01 to CH03 as derived from (a–c) version O and (d–f) version U calibration algorithms.

Table 6 Standard deviation of $NL_{c,k}$, i.e., $\sigma_{NL,c}$ (%), over detectors of columns one to three for ABI CH01 to CH03 derived from NSS field campaign data with version O and U calibration algorithms, respectively.

	Version O calibration			Version U calibration		
ABI channel	Col. #1	Col. #2	Col. #3	Col. #1	Col. #2	Col. #3
CH01	1.27	1.21	1.16	0.17	0.18	0.31
CH02	1.29	1.27	0.97	0.62	0.35	0.28
CH03	0.65	0.63	0.53	0.36	0.24	0.27

where $\overline{L_c}$ is the mean target radiance. $NL_{c,k}$ is the key parameter used to assess the detector uniformity for each ABI channel.

In Fig. 18, the color-coding for the scattered points in each panel indicates the column number for each detector of the corresponding channel. Several key points can be inferred from the comparison in Fig. 18.

a. The Q-scaling scheme paired with the new Q-LUT (version U) significantly reduces the detector-to-detector spread as can be seen from comparing the left and right columns in Fig. 18. This can also be inferred from the reduction in the standard deviation of NL, i.e., $\sigma_{NL,c}$ for detector column c ($c = 1, 2, 3$), as listed in Table 6. For ABI CH01, the reduction in σ_{NL} is the most significant (>4 times), which indicates that the detector uniformity was largely improved with the version U calibration algorithm. From Table 6, version U also significantly increases the detector-uniformity for ABI CH02 and CH03.
b. Comparing the NL data of version O and U in Fig. 18, it can be seen that the outliers with large deviations from mean NL values were removed in version U NSS data for ABI CH01, CH02, and CH03. This indicates that the destriping algorithm implemented in the version U solar calibration is quite successful.
c. Version U still has a residual rising slope of ~0.5% across detectors with a detector number <200 for ABI CH01. For ABI CH02, there is an apparent rapid rise in $NL_{c,k}$ for a detector number >1300, which might be due to the uncertainty in the prelaunch solar diffuser BRDF characterization. For ABI CH03, there is a residual downward slope of (~0.75%) in $NL_{c,k}$ for a detector number >400. It is worth of pointing out that the ability of identifying the residual slope across detectors with the NSS data can greatly assist the evaluation of the solar diffuser BRDF LUT used in the solar calibration. The remaining differences in the distribution of $NL_{c,k}$ data with different column numbers for the updated calibration algorithm (the right column of Fig. 18) might be due to the slight difference in the E/W scan-angle locations of these detectors with different column numbers.

4.3 *Detector Uniformity Evaluation from Reanalysis of GOES-16 ABI Lunar NSS Data*

4.3.1 *Lunar NSS of GOES-16 ABI*

During the GOES-16 postlaunch test (PLT) and postlaunch product test (PLPT) periods, the ABI lunar NSS was conducted over the Moon surface when the Moon transited across the space annulus within the ABI field of regard (FOR) and outside of the Earth disk. The same timeline 25 designed for the NSS of the Earth target was scheduled for the lunar NSS. In this section, the ABI CH01 to CH03 detector uniformity are evaluated with the lunar NSS data collected on April 10, 2017, and compared with the results from the NSS over land target analyzed in Sec. 4.2. Unlike the initial vendor-processing of timeline 25 NSS data collected during the field campaign, the lunar NSS data was processed from level-0 (raw data) and radiometrically calibrated by the

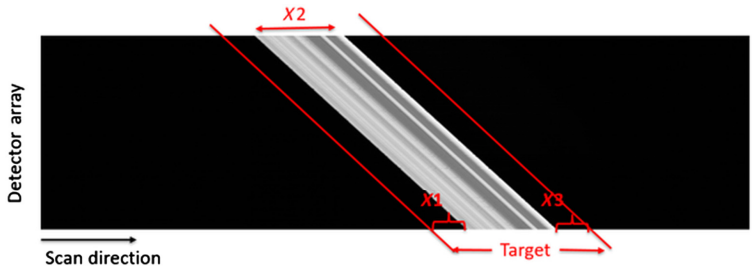

Fig. 19 Lunar NSS images for GOES-16 ABI CH03 derived from the lunar data collected on April 10, 2017. The *X*-axis is along the NSS direction, and the *Y*-axis direction is along the detector array direction. The lunar NSS target, shown as in-between the two red lines, is used for the ABI detector uniformity assessment. *X*2 is the number of the illuminated lunar samples along the scan direction of lunar NSS. *X*1 and *X*3 are the number of samples away from the lunar edges.

GOES-R calibration working group (CWG), which provides an independent validation of the NSS results over the Earth scenes.

To collect lunar NSS data, the north/south and east/west scan mirrors of ABI sensor were pointed to the middle of the space annulus around the Earth disk in the FOR of ABI that intercepts with the Moon's orbit. The lunar NSS started when the Moon moved into the FOR on the west side of the Earth. The NSS scheduled under ABI timeline 25 mode was continuously executed until the Moon was occluded by the Earth. The same procedure was repeated as the Moon reappeared in the space on the east side of the Earth. Because the Moon moves along east/west direction relative to the Earth due to the Earth's rotation and only one channel's detectors can be placed at the target location during NSS due to different detector locations of ABI channels on the focal plane, the lunar NSS of different ABI channels scan across different surface locations on the Moon. Figure 19 shows an example of a lunar NSS image of GOES-16 ABI CH03 collected on April 10, 2017. The *X*-axis is along the NSS direction of the ABI, and the *Y*-axis is the along the direction of the detector array. The lunar phase angle is ~6 deg and ~9 deg during the two NSS data collection events at the west and east side of Earth, respectively. Similar to the ABI NSS over the Earth target, the detectors from the same detector column in each ABI channel scanned across the same lunar surface and space areas. For each detector, the bright pixels along the *X*-axis in Fig. 19 are the illuminated lunar surface being scanned from north to south by the detector.

4.3.2 *ABI detector uniformity performance from reanalysis of lunar NSS data*

In this study, the ABI detector gain values were calculated using the two calibration algorithms introduced in Sec. 4.1 and then applied to the lunar NSS data to assess the detector uniformity of GOES-16 ABI CH01 to CH03. In particular, the detector linear gain (M) and nonlinear (Q) factor from the version O and U calibration algorithms were applied to convert the digital count data of the ABI lunar NSS collection to radiance data.

Different from the NSS of the Earth target, the lunar NSS has clean transitions from space to the Moon. To minimize the possible impacts from instrument blooming, stray light from the Earth and/or Moon, and scattering from Earth's atmosphere, the target area for the lunar NSS study is chosen to be composed of the illuminated lunar surface and the space surrounding the moon. Therefore, the target area for detector uniformity evaluation includes the following three regions as the ABI scans from the northern to the southern sides of the Moon (Fig. 19).

1. Samples in space to the northern side of the illuminated Moon (*X*1);
2. Illuminated lunar surface samples (*X*2);
3. Samples in space to the southern side of the Moon (*X*3).

In addition, to ensure a sufficient amount of lunar surface samples and average out the impacts due to the variation of the lunar surface reflectance along the scanning path of NSS, the lunar NSS with the largest number of illuminated pixels is selected for each ABI channel. The illuminated lunar boundaries along the scanning path of each detector are identified as

being at the first of the 10 consecutive samples that have radiance larger than the nominal radiance of space. The nominal radiance of space is defined as the mode value derived from the histogram of space radiance around the Moon.

The radiance $(L_{c,k})$ of the target region along the lunar NSS for detector k from detector column c (1, 2, and 3) of each ABI channel is calculated as

$$L_{c,k} = \sum_{i=0}^{X1} L_{c,k,i} + \sum_{i=0}^{X2} L_{c,k,i} + \sum_{i=0}^{X3} L_{c,k,i}, \tag{6}$$

where i is the pixel sample located within the $X1$, $X2$, and $X3$ segments along the scan direction shown in Fig. 19. The value of $X2$ is the number of illuminated lunar samples along the scan direction. $X1$ and $X3$ are the number of samples away from the northern and southern boundaries of the illuminated lunar surface, respectively. The reason for including sufficient samples away from Moon, i.e., over the $X1$ and $X3$ regions, is to calculate the moon-shine radiation into the vicinity of space. In this study, $X1$ and $X3$ are chosen to be 0.0013 radian away from the lunar edge. This ensures that no lunar radiation can be detected for all of the RSBs at samples beyond 0.0013 radian away from the lunar edge.

The mean target radiance for the detector k from column c is calculated as $\overline{L_{c,k}}$. The underlying basis for the detector uniformity validation with lunar NSS data is that all of the detectors from the same detector column (c) of a given ABI channel scan through and collect the data over the same target region on the Moon. Therefore, the detector uniformity performance for each channel is then evaluated by comparing the target radiance of each detector $(L_{c,k})$ to the mean target radiance $\overline{L_c}$, i.e., the normalized target radiance $\mathrm{NL}_{c,k}$.

Figure 20 shows the normalized target radiance ($\mathrm{NL}_{c,k}$) for each detector k in column c (color-coded) of ABI CH01 to CH03 as calculated with the version O (left column) and version U (right column) calibration algorithms, respectively. Table 7 shows the standard deviation of

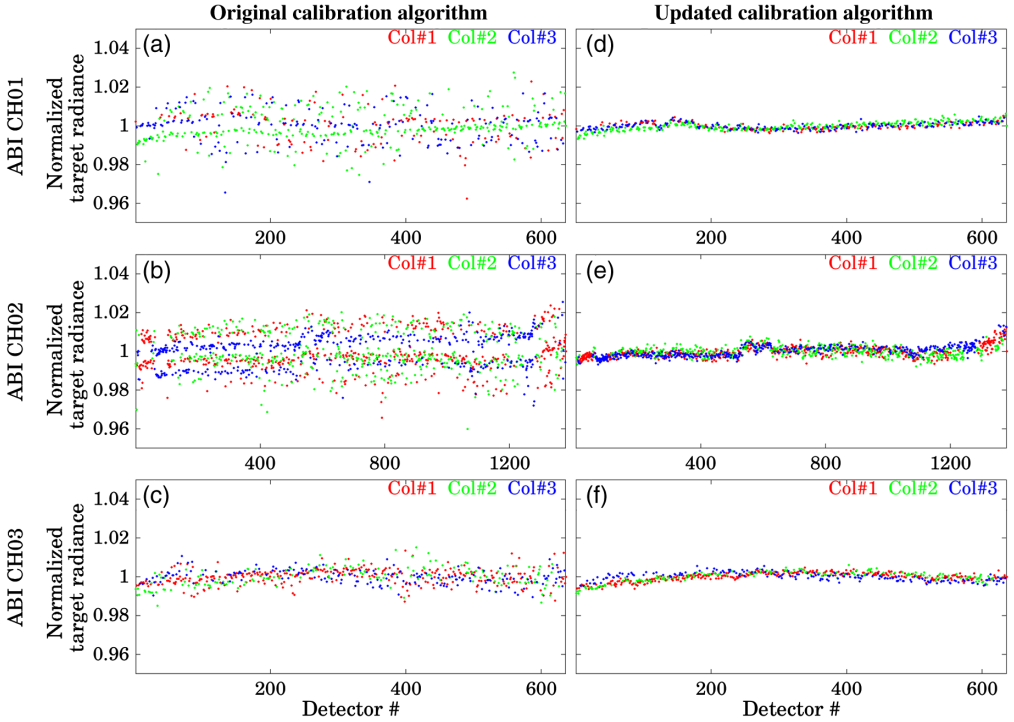

Fig. 20 Normalized lunar target radiance ($\mathrm{NL}_{c,k}$) for each detector k in column c (color-coded) calculated with (a–c) version O and (e–g) version U calibration algorithms for GOES-16 ABI CH01, CH02, and CH03, respectively.

Table 7 Standard deviation of $NL_{c,k}$, i.e., $\sigma_{NL,c}$ (%), over detectors of columns one to three for ABI CH01 to CH03 derived from lunar data with version O and U calibration algorithms, respectively.

	Version O calibration			Version U calibration		
ABI channel	Col. #1	Col. #2	Col. #3	Col. #1	Col. #2	Col. #3
CH01	0.97	0.87	0.88	0.18	0.22	0.16
CH02	1.04	1.02	0.82	0.30	0.25	0.30
CH03	0.41	0.51	0.38	0.22	0.28	0.22

Table 8 RMSE of normalized radiance difference between field campaign data (Fig. 18) and lunar data (Fig. 20) over detectors of columns one to three for ABI CH01 to CH03 processed with version O and U calibration algorithms.

	Version O calibration			Version U calibration		
ABI channel	Col. #1	Col. #2	Col. #3	Col. #1	Col. #2	Col. #3
CH01	3.92×10^{-3}	4.3×10^{-3}	4.09×10^{-3}	1.88×10^{-3}	1.93×10^{-3}	2.74×10^{-3}
CH02	4.88×10^{-3}	4.82×10^{-3}	3.36×10^{-3}	4.37×10^{-3}	3.80×10^{-3}	2.53×10^{-3}
CH03	4.65×10^{-3}	3.45×10^{-3}	2.57×10^{-3}	4.09×10^{-3}	2.97×10^{-3}	1.68×10^{-3}

$NL_{c,k}$, i.e., $\sigma_{NL,c}$ (%), for detectors of columns 1 to 3 for ABI CH01 to CH03 derived from lunar data.

We calculated the RMSE of normalized radiance difference between field campaign NSS data (Fig. 18) and lunar NSS data (Fig. 20) processed with two calibration algorithms. The results are shown in Table 8. The field campaign and lunar data shown in Figs. 18 and 20, respectively, are in general consistent with having RMSE within 5.0×10^{-3}.

As shown in Fig. 20, the $NL_{c,k}$ of ABI CH01 to CH03 derived from the version O algorithm has a strong detector-to-detector variation, which is consistent with the striping analysis results using the NSS scan image of the Earth shown in Fig. 18. The updated Q values in version U were derived based on the on-orbit measurements of the Earth scene and aimed at the remediation of the image striping and enhancing the detector uniformity. Figure 20 shows the independent validation of the reduction in the detector-to-detector variations after applying the version U calibration algorithm to the lunar NSS data of ABI CH01 to CH03. In addition, Fig. 20 shows that the lunar NSS data of version U confirm the removal of those outliers in version O for CH01, CH02, and CH03. All of these improvements are consistent with those in Fig. 18.

Similar to those shown in Fig. 18, rising slopes in CH01 and CH02 lunar NSS data processed with the version U calibration algorithm remain. Both lunar and Earth view data show different patterns for CH02 before the calibration algorithm update, i.e., the blue dots are divided into two bias groups in the left middle panels of Figs. 18 and 20, in comparison with the other two channels, e.g., CH01 and CH03. After the implementation of the updated calibration algorithm, such differences in scattering are removed as shown in the right column of Figs. 18 and 20. Both the land and lunar NSS data show that the NL data for detector number >1300 of the ABI CH02 detector array displays a rapid upward trend. This may be due to the uncertainty in the prelaunch characterization of the solar diffuser BRDF for ABI CH02.

The above analysis of GOES-16 ABI NSS data from field campaign and lunar observations demonstrates that the reanalysis of NSS data enables quantitative evaluation of the detector uniformity performance between calibration algorithms. Both the field campaign and lunar NSS data confirm the improvement in the detector uniformity in ABI CH01 to CH03 with the application of the updated Q LUT and Q-scaling scheme in solar calibration. The NSS data can also quantify the residual slope across detectors, which may be traced back to the uncertainty in the

solar diffuser BRDF used in the solar calibration. The consistency in the detector uniformity performance between land and lunar NSS data also assures the robustness of the NSS data in evaluating the detector uniformity performance for ABI RSB channels.

In Ref. 35, a striping mitigation method for the RSB channels of GOES-R ABI using NSS data was demonstrated. In Ref. 36, a striping detection and characterization method for ABI Earth view images was developed. Based on this method, the striping performance of the operational GOES-16 ABI Level-1B Earth view data products are closely monitored at Ref. 37. The improvements of the GOES-16 ABI striping performance over Earth observations from the version O to U calibration algorithms during the timeline shown in Table 5 can also be monitored from this web page. We also note that, from the analysis in Refs. 36 and 38 and online striping monitoring page, GOES-16 ABI CH04 to CH06 images perform well, and the striping in these channels is of less concern than in ABI CH01 to CH03. Therefore, nonlinear Q calibration LUTs were not entirely updated for ABI CH04 to CH06.

5 Summary

In this paper, the radiometric biases and uncertainties of RSB and TEB of the GOES-16 ABI have been evaluated through comparison with independent airborne reference sensor measurements collected by AVIRIS-NG and S-HIS, respectively, during the field campaign on March 28, 2017. In addition, the detector uniformity performance of GOES-16 ABI CH01 to CH03 was evaluated with the NSS data collected during both the field campaign and lunar scans and was processed with two calibration algorithms.

Through intercomparison between GOES-16 ABI RSB and AVIRIS-NG measurements over co-located targets in the Sonoran Desert region on March 28, 2017, the radiometric biases of ABI RSB were evaluated. In comparison with AVIRIS-NG measurements, the mean radiometric biases for ABI CH01, Ch03, CH05, and CH06 determined from MESO data were all within 2% with total uncertainty <2.5%. The total uncertainty was SI traceable to NIST via a FEL lamp. The radiometric biases $\pm$ uncertainties for all five ABI RSB channels studied in this paper were within the 5% radiometric accuracy requirement. For ABI CH02, the MESO data comparison with AVIRIS-NG data showed $\sim$2.85% $\pm$ 2.15% positive bias, which could be due to detector nonuniformity as shown in Fig. 18(b). The comparison with NSS data for ABI CH02 in Ref. 17 showed $\sim$7% positive bias, which is closer to the $\sim$6.4% bias determined from the independent analysis with GOES-16 ABI and SNPP VIIRS collocation data.[4,29–32] The possible cause of the particularly large bias for ABI CH02 can be due to the uncertainty in the solar diffuser reflectance table determined in the prelaunch test. The mitigation of ABI CH02 bias was implemented on April 23, 2019, using a rescaled the solar diffuser reflectance table and the resulting radiometric bias of GOES-16 ABI CH02 was reduced by $\sim$6.4%.[4,31,32]

The BT differences between GOES-16 ABI TEB and S-HIS measurements over colocated land targets in the Sonoran Desert region on March 28, 2017, are also compared. In comparison with S-HIS, GOES-16 ABI CH08 to CH11 have positive BT biases <0.55 K with uncertainties <0.35 K and ABI CH13 to CH15 have negative BT bias with amplitude being <0.45 K and uncertainties <0.3 K at the 300 K BT scene equivalent. The overall BT biases of ABI CH08 to CH11 and CH13 to CH15 determined from land scene in this paper are consistent in both sign and magnitude with those determined from the measurements over ocean on April 13, 2017, in Ref. 27. This is also consistent with TEB bias evaluation results from the GEO-LEO comparison between GOES-16 TEB and hyperspectral infrared measurement by the CrIS sensor on board SNPP and NOAA-20.[34] The bias of ABI CH07 was 0.97 K over land surface in comparison with S-HIS whereas the bias determined from S-HIS measurements over ocean was 0.24 K,[27] which can be due to the high emissivity and surface feature variability over land surface for this channel. GOS-16 ABI CH16 has a negative BT bias $\sim$1 K, which is due to the CO_2 absorption above the ER2 aircraft. The much larger bias of ABI CH12 (9.6 μm) is due to the ozone absorption above the ER2. For ABI CH12 and CH16, RTM corrections need to be applied to account of the atmosphere absorption above the aircraft to reconcile the BT difference between ABI and S-HIS measurements.

It is noted that GOES-16 ABI calibrations [including image navigation registration (INR) and radiometric calibrations] have evolved and improved after March 28, 2017, such that the radiometric bias analysis in this paper is an evaluation of data quality at the time, not necessarily representative of the overall quality achieved later.

This paper also developed a scheme to analyze ABI NSS data to address the challenge of evaluating the detector uniformity for ABI channels with hundreds to more than a thousand detectors. The NSS data collected during the field campaign and lunar observation were processed to evaluate the detector uniformity performance for ABI CH01 to CH03. Through the reanalysis of the ABI CH01 to CH03 NSS data with two calibration algorithms, the ABI NSS data from field campaign and lunar observation both showed significant improvements in detector uniformity due to the implementation of the Q-scaling scheme and the updated Q factor-LUT in the solar calibration. In particular, there were significant reductions in detector-to-detector variability and the removal of outliers after applying the Q-scaling scheme in the solar calibration together with the updated nonlinear calibration factor Q. It was also shown that there are residual slopes across detectors of ABI CH01 to CH03 after applying the version U solar calibration algorithm to process the NSS data from both the land and lunar observations. This residual slope might be due to the uncertainty in the prelaunch BRDF of the solar diffuser used in the solar calibration, which needs further investigation.

In summary, the field campaign provided an invaluable independent radiometric validation for GOES-16 ABI TEBs and RSBs. Through coordinated postlaunch field collections, the SI-traceable airborne spectral radiance measurements by AVIRIS-NG and S-HIS, together with the ray-matched GOES-16 ABI measurements, were made available. The comparison between GOES-16 ABI and AVIRIS-NG/S-HIS measurements enabled the validation of the SI traceability of the radiometric quality of the ABI level-1B RSB and TEB channels. The reanalysis of NSS data demonstrates its usefulness in evaluating calibration algorithm performance in terms of detector uniformity and identifying residual slope among detectors. The consistency in the detector uniformity performance from the land and lunar NSS data also assures their robustness for evaluation of ABI channels. It is also suggested that routine collection and analysis of NSS data of Moon or Earth targets can help monitor and trend the ABI detector-uniformity variation. In particular, the ABI CH04 is a water vapor absorption band and can be largely affected by the absorption. Because there is no atmosphere on the Moon, the lunar NSS data can provide a unique opportunity for the evaluation of detector uniformity of ABI CH04 (preliminary analysis results can be found in Ref. 38). It is further suggested that the NSS data can be further used to perform calibration of ABI detectors and reduce the striping. Performing actual radiometric calibration of ABI detectors and correct striping using NSS data will require deriving both linear and nonlinear calibration coefficients for each detector relative to a reference detector. This will further require the intercomparison of the NSS data of different detectors in the form of scatter or histogram plots to derive the relative linear/nonlinear coefficients. This analysis will also help with the selection of the best ABI detectors with optimal performance in nonlinearity and uncertainty to be used in the operational data production.

Acknowledgments

This study was supported by NOAA (Grant No. NA19NES4320002) (Cooperative Institute for Satellite Earth System Studies—CISESS) at the University of Maryland/ESSIC. We thank the AVIRIS-NG Team for operating the AVIRIS-NG instrument during the field campaign and making the data available. We thank Joe Taylor and S-HIS Team (University of Wisconsin-Madison) for operating the S-HIS instrument during the field campaign and making the data available. We also thank Brent Bartlett and Jason Casey for helpful discussions. We thank the GOES-R ABI Trending and Data Analysis Toolkit (GRATDAT) team for developing the tool to ingest the ABI Level-0 data. The scientific results and conclusions, as well as any views or opinions expressed herein, are those of the author(s) and do not necessarily reflect those of NOAA or the Department of Commerce. The authors have no relevant financial interests in the manuscript and no other potential conflicts of interest to disclose.

References

1. J. P. Fulbright et al., "Calibration/validation strategy for GOES-R L1b data products," *Proc. SPIE* **10000**, 100000T (2016).
2. R. Datla et al., "Comparison of the calibration algorithms and SI traceability of MODIS, VIIRS, GOES, and GOES-R ABI sensors," *Remote Sens.* **8**, 126 (2016).
3. T. J. Schmit et al., "A closer look at the ABI on the GOES-R series," *Bull. Am. Meteorol. Soc.* **98**, 681–698 (2017).
4. F. Yu et al., "Early radiometric calibration performances of GOES-16 advanced baseline imager," *Proc. SPIE* **10402**, 104020S (2017).
5. F. Yu et al., "Validation of early GOES-16 ABI on-orbit geometrical calibration accuracy using SNO method," *Proc SPIE* **10402**, 104020U (2017).
6. X. Shao, X. Wu, and F. Yu, "Stray-light performance comparison between Himawari-8 AHI and GOES-16 ABI," in *IEEE Int. Geosci. and Remote Sens. Symp. (IGARSS)*, Fort Worth, Texas, pp. 286–289 (2017).
7. S. Kalluri et al., "From photons to pixels: processing data from the advanced baseline imager," *Remote Sens.* **10**(2), 177 (2018).
8. R. Iacovazzi et al., "GOES-16 advanced baseline imager instrument performance monitor," *J. Appl. Remote Sens.* **14**(1), 016512 (2020).
9. X. Shao et al., "Characterization and monitoring of GOES-16 ABI stray light and comparison with Himawari-8 AHI and GOES-17 ABI," *J. Appl. Remote Sens.* **15**(1), 017503 (2021).
10. J. V. Naarden and D. Lindsey, "Saving GOES-17," 2019, https://aerospaceamerica.aiaa.org/departments/saving-goes-17 (accessed 14 July 2022).
11. Z. Wang et al., "On-orbit calibration and characterization of GOES-17 ABI IR bands under dynamic thermal condition," *J. Appl. Remote Sens.* **14** (3), 034527 (2020).
12. S. Ungar et al., "Data quality guidelines for GEOSS consideration-the CEOS Working Group on Calibration and Validation (WGCV)," in *IEEE Int. Geosci. and Remote Sens. Symp.*, pp. 306–309 (2007).
13. M. Goldberg et al., "The global space-based inter-calibration system," *Bull. Am. Meteorol. Soc.* **92**, 467–475 (2011).
14. F. Padula et al., "Towards post-launch validation of GOES-R ABI SI traceability with high-altitude aircraft, small near surface UAS, and satellite reference measurements," *Proc. SPIE* **99720** (2016).
15. F. Padula et al., "GOES-R Advanced Baseline Imager (ABI) and Geostationary Lightning Mapper (GLM) calibration/validation from a field campaign perspective," in *Proc. IGARSS, New GEO/LEO Mission Adv. Imagery Products: Opt. Sens. Calibration and Appl. II MO4.L8.3* (2017).
16. J. T. Casey et al., "Characterization of GOES-16 ABI detector-level uniformity from post-launch north south scan collections of several earth targets," *Proc. SPIE* **10764**, 107640D (2018).
17. B. Bartlett et al., "Independent validation of the advanced baseline imager (ABI) on NOAA's GOES-16: post-launch ABI airborne science field campaign results," *Proc. SPIE* **10764**, 107640H (2018).
18. X. Shao et al., "Validation of GOES-16 ABI reflective solar band calibration through reanalysis and comparison with field campaign data," *Proc. SPIE* **10764**, 107640I (2018)
19. L. Hamlin et al., "Imaging spectrometer science measurements for terrestrial ecology: AVIRIS and new developments," in *Aerosp. Conf.*, IEEE (2011).
20. D. R. Thompson et al., "Atmospheric correction with the Bayesian empirical line," *Opt. Express* **24**, 2134 (2016).
21. D. R. Thompson et al., "Optimal estimation for imaging spectrometer atmospheric correction," *Remote Sens. Environ.* **216**, 355–373 (2018).
22. J. W. Chapman et al., "Spectral and radiometric calibration of the next generation airborne visible infrared spectrometer (AVIRIS-NG)," *Remote Sens.* **11**, 2129 (2019).
23. W. McMillan et al., "Tropospheric carbon monoxide measurements from the scanning high-resolution interferometer sounder on 7 September 2000 in southern Africa during SAFARI 2000," *J. Geophys. Res.* **108**, 8492 (2003).

24. J. Taylor et al., "Performance of an infrared sounder on several airborne platforms: the scanning high resolution interferometer sounder (S-HIS)," *Proc. SPIE* **5882**, 588214 (2005).
25. D. Tobin et al., "Radiometric and spectral validation of atmospheric infrared sounder observations with the aircraft-based scanning high-resolution interferometer sounder," *J. Geophys. Res.* **111**, D09S02 (2006).
26. J. Taylor et al., "The scanning high-resolution interferometer sounder (S-HIS)," in ARM Aerial Instrument Workshop Report, 2020, https://www.arm.gov/publications/programdocs/doe-sc-arm-20-010.pdf (accessed 14 July 2022).
27. J. Taylor et al., "Calibration validation of the GOES-16 advanced baseline imager (ABI) with the high-altitude aircraft based scanning high-resolution interferometer sounder (S-HIS)," in *Opt. Sens. and Sens. Congr. (ES, FTS, HISE, Sensors)*, OSA Technical Digest, p. FTu2B.2 (2019).
28. https://ncc.nesdis.noaa.gov/GOESR/ABI.php (accessed 14 July 2022).
29. S. Uprety, C. Cao, and X. Shao, "Geo-Leo intercalibration to evaluate the radiometric performance of NOAA-20 VIIRS and GOES-16 ABI," *Proc. SPIE* **11127**, 111270S (2019).
30. R. Bhatt et al., "Advances in utilizing tropical deep convective clouds as a stable target for on-orbit calibration of satellite imager reflective solar bands," *Proc. SPIE* **11127**, 111271H (2019).
31. S. Uprety, C. Cao, and X. Shao, "Radiometric consistency between GOES-16 ABI and VIIRS on Suomi NPP & NOAA-20," *J. Appl. Remote Sens.* **14**(3), 032407 (2020).
32. X. Jing et al., "Validation of GOES-16 ABI VNIR channel radiometric performance with NPP and NOAA-20 VIIRS over the Sonoran Desert," *J. Appl. Remote Sens.* **14**(4), 044517 (2020).
33. J. McCorkel et al., "GOES-16 ABI solar reflective channel validation for earth science application," *Remote Sens. Environ.* **237**, 111438 (2019).
34. F. Yu et al., "Radiometric calibration accuracy and stability of GOES-16 ABI infrared radiance," *J. Appl. Rem. Sens.* **15**(4), 048504 (2021).
35. M. Cook et al., "Reflective solar band striping mitigation method for the GOES-R series advanced baseline imager using special scans," *J. Appl. Remote Sens.* **14**(3), 032409 (2020).
36. H. Qian et al., "Detection and characterization of striping in GOES-16 ABI VNIR/IR bands," *Proc. SPIE* **10764**, 107641N (2018).
37. https://www.star.nesdis.noaa.gov/GOESCal/G16_ABI_StripingAll_daily.php (accessed 14 July 2022).
38. F. Yu et al., "Applications of GOES-16 ABI Lunar North-South Scan (NSS): detector out-of-field, blooming, and uniformity responses," in CalCon Technical Meeting, Logan, Utah, 2018, https://digitalcommons.usu.edu/calcon/CALCON2018/all2018content/23/ (accessed 14 July 2022).

Xi Shao received his BS degree in space physics from the University of Science and Technology of China, in 1996. He received his PhD in astronomy and his MS degree in electrical engineering in microelectronics major, both from the University of Maryland, College Park, USA, in 2001 and 2004, respectively. Currently, he is a research scientist at Cooperative Institute for Satellite Earth System Studies (CISESS) and Department of Astronomy, University of Maryland. He has authored/coauthored over 80 scientific journal publications in various research areas.

Changyong Cao is a supervisory physical scientist at the NOAA Center for Satellite Applications and Research. He specializes in the calibration of radiometers on board NOAA's Operational Environmental Satellites, and currently leads the VIIRS sensor science team. He was the recipient of three gold and one silver medals honored by the U.S. Department of Commerce for his scientific and professional achievements. He received his PhD from Louisiana State University in 1992.

Xiangqian Wu coleads the GOES-R Calibration Working Group (CWG) at NOAA in Maryland, United States, specializing in ABI calibration. He has led the operational calibration for NOAA's AVHRR on POES since 2002, the imager and sounder on GOES since 2004, and OMPS on S-NPP between 2010 and 2014. He has been a member of the WMO-sponsored

Global Space-based Inter-Calibration System (GSICS) Research Working Group since its inception and served as its first chair.

Fangfang Yu is the lead of the GOES-R ABI cal/val support team at the Cooperative Institute for Climate and Satellites, University of Maryland, supporting the operational calibration of NOAA's GOES imaging instruments. She has been supporting and working on the calibration and validation of NOAA's operational optical instruments since 2005. Her major research interests focus on the radiometric calibration and validation of the geostationary weather satellite instruments.

Haifeng Qian is an associate research scientist in CISESS/ESSIC of University of Maryland, College Park. Before he obtained his master's degree in 2005 and PhD in 2008 in University of Maryland, he received his bachelor's degree in 1999 and master's degree in 2002 in Nanjing University, China. His main research activities are in the fields of satellite calibration, validation and climate dataset record development and application, climate modeling, data analysis and mining.

Biographies of the other authors are not available.